

Fermion-to-Fermion Low-Density Parity-Check Codes

Chong-Yuan Xu^{1,*}, Ze-Chuan Liu^{1,*}, and Yong Xu^{1,2†}

¹Center for Quantum Information, IIIS, Tsinghua University, Beijing 100084, People's Republic of China and

²Hefei National Laboratory, Hefei 230088, People's Republic of China

Simulating fermionic systems on qubit-based quantum computers often demands significant computational resources due to the requirement to map fermions to qubits. Thus, designing a fault-tolerant quantum computer that operates directly with fermions offers an effective solution to this challenge. Here, we introduce a protocol for fault-tolerant fermionic quantum computation utilizing fermion-to-fermion low-density parity-check (LDPC) codes. Our method employs a fermionic LDPC memory, which transfers its state to fermionic color code processors, where logical operations are subsequently performed. We propose using odd-weight logical Majorana operators to form the code space, serving as memory for the fermionic LDPC code, and provide an algorithm to identify these logical operators. We present examples showing that the encoding rate of fermionic codes often matches that of qubit codes, while the logical failure rate can be significantly lower than the physical error rate. Furthermore, we propose two methods for performing fermionic lattice surgery to facilitate state transfer. Finally, we simulate the dynamics of a fermionic system using our protocol, illustrating effective error suppression.

The study of strongly correlated fermionic systems is central to high-energy physics [1], material science [2], and quantum chemistry [3], promising insights into phenomena ranging from quark dynamics [4] to high-temperature superconductivity [5]. However, solving these problems using classical computers is often very challenging. For instance, quantum Monte Carlo methods usually face the sign problem when addressing fermionic problems [6]. In this context, quantum computers offer a promising alternative [7]. However, since conventional quantum computers use qubits, solving fermionic problems requires mapping fermionic operators to qubit operators, which often incurs substantial overhead [8–13], making experimental implementation significantly challenging in the near term. To address this challenge, developing programmable fermionic quantum processors is increasingly appealing [10, 14]. In light of the unavoidable presence of noise, fault-tolerant fermionic quantum computing based on fermion-to-fermion repetition and color codes have been proposed very recently [15, 16]. However, the protocol's overhead remains substantial because the encoding rate is low, with each block encoding only a single logical fermion.

Recently, protocols based on quantum LDPC codes have been proposed to reduce the overhead in qubit-based fault-tolerant quantum computation [17–40]. Compared to the paradigmatic surface code, quantum LDPC codes feature a significantly higher encoding rate. Although these codes require long-range connectivity between qubits, recent technological advances in platforms [38, 41–44] such as Rydberg atom arrays, superconducting qubits, and trapped ions have made the near-term implementation of these codes promising. Despite these significant advancements, existing studies primarily focus on constructing fault-tolerant quantum computers with qubits. It remains unclear how to construct a fermion-to-fermion LDPC code capable of encoding mul-

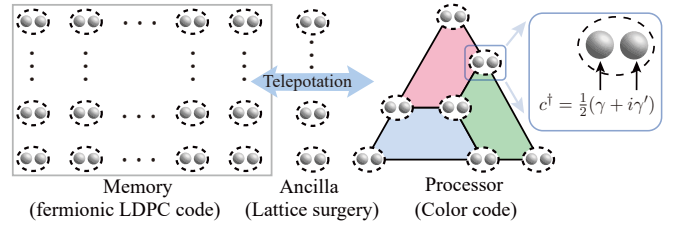


FIG. 1. Schematic illustration of fault-tolerant fermionic quantum computation framework. The architecture comprises three components: fermionic memory implemented using fermionic LDPC codes, fermionic processor implemented using fermionic color codes to execute logical operations, and fermionic interface composed of ancilla fermions serving as a critical bridge for communication between memory and processor.

multiple fermion modes in a single code block and how to perform logical operations on such codes.

Here, we introduce a protocol for fault-tolerant fermionic quantum computation based on fermion-to-fermion LDPC codes. Our approach employs a fermionic LDPC memory integrated with fermionic color code processors as illustrated in Fig. 1, which is generalized from the quantum LDPC case [37]. Logical fermionic information is initially stored in the fermionic LDPC memory and, when needed, is transferred to fermionic color code processors, where fault-tolerant logical operations are conducted. Upon completion, the information is returned to the memory. To construct the fermionic LDPC memory, we develop a systematic workflow for creating fermionic stabilizer codes based on weakly-self-dual Calderbank-Shor-Steane (CSS) codes. These codes are characterized by logical Majorana operators consisting of an odd number of physical Majorana operators. We construct four distinct classes of fermionic LDPC codes using four different weakly-self-dual LDPC codes: bicycle codes [45], finite Euclidean geometry codes [46, 47],

finite projective geometry codes [48] and stacked LDPC codes [49]. These codes can have a significantly higher encoding rate compared to the fermionic color code. Furthermore, we propose two methods for performing fermionic lattice surgery to facilitate transfer of logical fermionic states between the fermionic memory and processor. We show that this process maintains the code distance. Finally, we simulate the dynamics of a fermionic system, demonstrating effective error suppression.

We start by introducing the construction of our fermionic LDPC codes from $2n$ physical Majorana fermion operators $\{\gamma_1, \gamma'_1, \gamma_2, \gamma'_2, \dots, \gamma_n, \gamma'_n\}$ arising from n physical complex fermions' creation and annihilation operators [50]. The strings of these Majorana operators, together with a phase factor $\eta \in \{\pm 1, \pm i\}$, generate the group of Majorana operators $\text{Maj}(2n) \equiv \left\{ \Gamma = \eta \prod_{j=1}^n \gamma_j^{\alpha_j} (\gamma'_j)^{\alpha'_j} | \alpha_j, \alpha'_j \in \{0, 1\} \right\}$ [51]. The number of Majorana operators in Γ is referred to as its weight. The Majorana stabilizer code is defined by a Majorana stabilizer group \mathcal{S}_{maj} , a subgroup of $\text{Maj}(2n)$, where all elements are Hermitian, mutually commute, ensuring it is an Abelian subgroup, have even weight to preserve the parity of a physical fermion system, and $-I$ with I being the identity element in the group is excluded [51]. The logical operators are generated by an independent subset of $\text{Maj}(2n)$ comprising Majorana operator strings that commute with all elements of the stabilizer group \mathcal{S}_{maj} but are not members of \mathcal{S}_{maj} [52].

Each Majorana string operator can be represented by a binary vector $(\alpha_1, \alpha'_1, \dots, \alpha_n, \alpha'_n)$, where $\alpha_j, \alpha'_j \in \{0, 1\}$ and $1 \leq j \leq n$. The binary vectors corresponding to the m independent stabilizer generators of \mathcal{S}_{maj} form an $m \times 2n$ check matrix. For a fermion-to-fermion LDPC code, we construct a check matrix H based on a weakly-self-dual CSS code with the binary check matrices that satisfy $H_X = H_Z = A$ and $AA^T = 0$, as follows,

$$H = \begin{pmatrix} H_\gamma & 0 \\ 0 & H_{\gamma'} \end{pmatrix}, \quad (1)$$

where $H_\gamma = H_{\gamma'} = A$. H_γ and $H_{\gamma'}$ correspond to check matrices that characterize the stabilizers consisting exclusively of $\{\gamma_j\}$ and $\{\gamma'_j\}$ operators, respectively, as described for fermion-to-fermion color codes in Ref. [15]. The logical operators are represented by vectors in the kernel of H that cannot be generated by stabilizers, whose span forms a homology group $\ker(A)/\text{im}(A^T)$ for both γ and γ' types of logical operators [53].

In our protocol, there are multiple logical fermion modes within a single fermionic LDPC memory, and these logical fermion modes are transferred to processors for the execution of logical operations. It is essential that the logical Majorana operator in memory anticommutes with that in the processor to adhere to fermionic statistics. We thus require all logical Majorana operators in memory have odd weight and even overlap with each

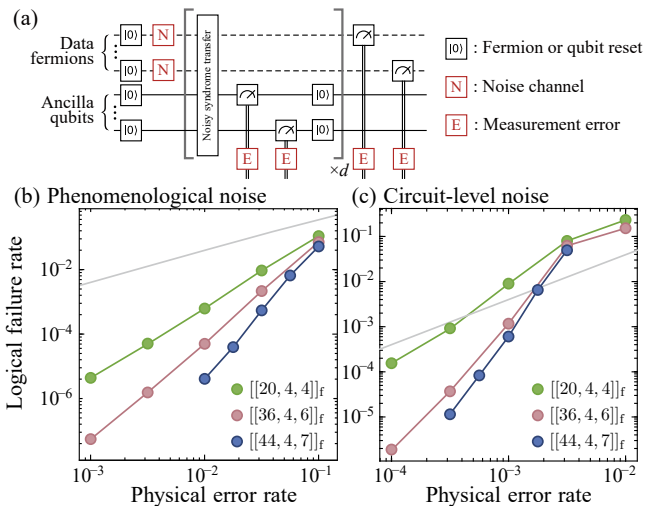


FIG. 2. (a) Illustration of the circuit-level noise model where the syndrome extraction transfer circuits used to establish entanglement between data fermions and ancilla qubits are noisy. The initial states are physical $|0\rangle$ states for fermions. In the end, a transversal measurement on all physical fermion modes in the particle number basis is performed. Logical failure rate p_L versus physical error rate p under (b) phenomenological and (c) circuit-level noise model for fermionic $[[20, 4, 4]]_f$, $[[36, 4, 6]]_f$ and $[[44, 4, 7]]_f$ double-chain bicycle codes. We also perform a power law fit to the data according to the fitting formula $p_L \sim p^\alpha$ with $\alpha = 2.21, 3.06, 4.3$ in (b) and $\alpha = 2.12, 3.46, 4.54$ in (c), and the gray lines represent the probability that at least an error occurs on four physical fermion modes. Here, the Tesseract decoder [54] is employed, and the results obtained using the belief propagation and ordered-statistical decoding (BP+OSD) [55, 56] algorithm are presented in Supplemental Material.

other [51]. Such conditions also ensure that the fermionic statistics are maintained when concatenating different fermion code blocks [15]. We denote the logical Majorana operators as $\bar{\gamma}_j$ and $\bar{\gamma}'_j$ with $1 \leq j \leq k$ (k is the number of logical complex fermion modes), which consist of physical Majorana operators $\{\gamma_1, \dots, \gamma_n\}$ and $\{\gamma'_1, \dots, \gamma'_n\}$, respectively. The logical complex fermion creation operators are then defined as $\bar{c}_j^\dagger = \frac{1}{2}(\bar{\gamma}_j + i\bar{\gamma}'_j)$ [50].

Previous studies have primarily focused on encoding Majorana modes into qubits [51, 57, 58]. While some results also demonstrate the existence of odd-weight logical operators in Majorana surface codes [59], there is a lack of methods for systematically identifying these operators within a fermionic LDPC code. To identify them, we generalize the Gram-Schmidt orthogonalization process to vector spaces over \mathbb{F}_2 [60]. Let $\{\bar{\gamma}_j | j = 1, \dots, k', k' \geq k\}$ be a basis for $\ker A / \text{im}(A^T)$, which is itself also a vector space; $\bar{\gamma}_j$ represents the corresponding logical $\bar{\gamma}_j$ or $\bar{\gamma}'_j$ operator, expressed as $\gamma_1^{[\bar{\gamma}_j]_1} \dots \gamma_n^{[\bar{\gamma}_j]_n}$ or $(\gamma'_1)^{[\bar{\gamma}_j]_1} \dots (\gamma'_n)^{[\bar{\gamma}_j]_n}$. If there exists a basis vector with odd number of 1's, say $\bar{\gamma}_1$, we remove it from the basis and make the remaining basis vectors

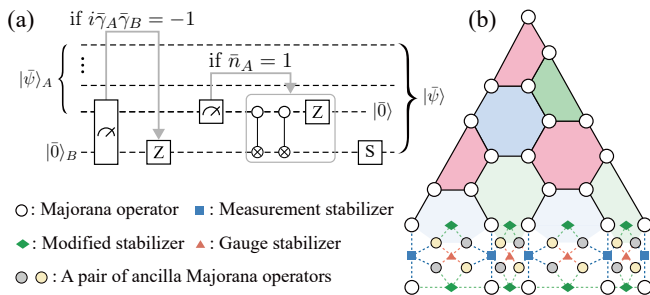


FIG. 3. (a) Quantum circuit to transfer a logical fermionic state $|\bar{\psi}\rangle_A$ to code block B (initialized as $|\bar{0}\rangle_B$). The protocol involves: (i) measuring $i\bar{\gamma}_A\bar{\gamma}_B$ and applying the Z gate of $\exp(i\pi\bar{n}_B)$, provided the measurement result is -1 ; (ii) measuring the logical particle number \bar{n}_A and applying two braiding gates and one fermionic Z gate, if the measurement outcome is 1 ; (iii) applying a phase rotation S gate to the state in the processor. The validation of this circuit is provided in Supplemental Material. (b) Illustration of the first method for lattice surgery achieving fault-tolerant measurements of $i\bar{\gamma}_A\bar{\gamma}_B$ in the case with $|\bar{\gamma}_A| = |\bar{\gamma}_B|$. In this example, code B is a $d = 5$ fermionic color code, and code A is a fermionic LDPC code containing five Majorana operators in the support of $\bar{\gamma}_A$. The empty circles represent the γ -type Majorana operators in blocks A and B . Several pairs of ancilla Majorana operators are introduced with each horizontal pair represented by yellow and gray circles to denote γ -type and γ' -type Majorana operator forming a complex fermion. The γ -type stabilizer generators at the boundary, connected to ancilla fermions, are modified to incorporate the ancilla Majorana operators (green rhombuses). Measurement and gauge stabilizer generators are depicted as blue squares and red triangles, respectively. The product of these stabilizer generators yields the joint logical operator $i\bar{\gamma}_A\bar{\gamma}_B$. The γ' -type Majorana stabilizers remain unchanged.

orthogonal to it via $\vec{\gamma}_j \rightarrow \vec{\gamma}_j - (\vec{\gamma}_1 \cdot \vec{\gamma}_j)\vec{\gamma}_1$, i.e., $\vec{\gamma}_1$ has even overlap with all others. This procedure is repeated until no odd-weight basis vector remains. The obtained odd-weight vectors correspond to logical operators which have odd weight, and the overlap weight between any two of them is even, thus satisfying the fermionic anticommutation relation. The necessary and sufficient condition for the existence of at least one odd-weight logical is $(1, 1, \dots, 1)^T \notin \text{im}(A^T)$ [51]. We find that for all cases we consider, the procedure produces a linearly independent set containing k' odd-weight binary vectors (see Supplemental Material).

Based on four different LDPC codes, which include finite projective geometry codes [48], finite Euclidean geometry codes [46, 47], bicycle codes [45], and stacked LDPC codes [49], we construct four classes of fermionic LDPC codes, which yield the same code parameters $[[n, k, d]]_f$ as the original qubit codes (see Supplemental Material). We now focus on three fermionic double-chain bicycle codes, which belong to the fermionic stacked LDPC codes, and evaluate their logical information resilience as a fermion memory through numerical simu-

lations. Specifically, we initialize all physical fermion modes in the vacuum state, $|0\rangle$. The performance of a code depends on quantum error models employed. For completeness, we consider three types of error models, analogous to the qubit case: code-capacity, phenomenological and circuit-level error models (see Fig. 2(a)) [61]. The code-capacity error model does not account for errors in syndrome measurements and thus represents the upper bound of code performance against the errors considered. In the phenomenological and circuit-level error models, the syndrome measurement circuits are noisy: In the former, only the measurement outcomes are noisy, whereas in the latter, all operations in the circuit are also noisy (see Supplemental Material). Under these two error models, we perform $N_c = d$ rounds of syndrome measurements, followed by a transversal measurement on all physical fermion modes in the particle number basis, as illustrated in Fig. 2(a). We then apply a decoder to interpret the obtained syndromes and verify whether logical errors occur.

In numerical experiments, we perform N_{sample} trials and identify N_{error} erroneous occurrences. Consequently, the logical error probability is given by $P_L(N_c) = N_{\text{error}}/N_{\text{sample}}$. Conventionally, the logical failure rate is defined as $p_L = 1 - (1 - P_L(N_c))^{1/N_c} \approx P_L/N_c$ [37, 38], which approximately characterizes the logical error rate per syndrome cycle.

Figure 2(c) and (d) show the logical failure rate with respect to the physical error rate p for three fermionic double-chain bicycle codes. We clearly see that the logical failure rate is significantly suppressed compared to the physical one according to $p_L \sim p^\alpha$ with $\alpha \approx \lceil \frac{d}{2} \rceil$. By convention [38], we define the code's pseudo-threshold as the solution to the break-even equation $p_L(p) = P(p, k)$, where $P(p, k) = 1 - (1 - p)^k$ is the probability of at least one error occurring on k physical fermion modes at physical error rate p . Under the circuit-level error model, the calculated pseudo-thresholds of the $[[36, 4, 6]]_f$ and $[[44, 4, 7]]_f$ codes exceed 0.1%.

In Supplemental Material, we also provide the numerical simulation results for fermionic finite projective geometry codes, fermionic finite Euclidean geometry codes, fermionic bicycle codes, fermionic double-layer bivariate bicycle (BB) codes, fermionic double-layer twisted BB codes, and fermionic double-layer reflection codes. In addition, we study several other self-dual codes such as Kitaev Majorana code [50] and unicycle codes [45] and find that they are not suitable for producing well-behaved fermionic LDPC because they do not support the generation of odd-weight logical operators.

We now study how to perform logical operations on the fermionic LDPC memory. Instead of executing logical gates directly on the fermionic LDPC, we consider a method whereby the states of a target logical fermion mode in memory are transferred to an external fermionic color code processor. Logical operations are then per-

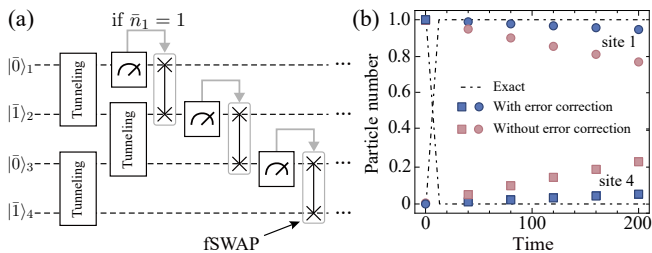


FIG. 4. (a) Quantum circuit used to benchmark our protocol. We first initialize the system in the logical state $|0101\rangle$ and then apply three tunneling gates with each gate executing the operation $T_{j,j+1} = \exp(i\pi(\bar{c}_j^\dagger \bar{c}_{j+1} + \text{H.c.})/2)$. Onsite measurements of $\bar{n}_j = \bar{c}_j^\dagger \bar{c}_j$ with $j = 0, 1, 2$ are then performed, followed by a fermionic swap (fSWAP) gate if the measurement result is zero. The unitary gates and feedback process constitute a module, which is executed consecutively multiple times. (b) The expectation value of logical particle numbers at site 1 and 4 with respect to time which is characterized by the number of executed modules. We see that the simulation under circuit-level noise with error correction (filled blue circles and squares) is close to the noiseless simulation result (the dotted-dashed lines), in stark contrast to the simulation results under noise without error correction (filled red circles and squares). In the simulation, we apply the first method for lattice surgery. Results using the second method are provided in the Supplemental Material. Here, we set the physical error rate $p = 10^{-4}$. The error bars are hidden behind the symbols.

formed on these processors, and the states are subsequently transferred back to the memory. This approach is inspired by fault-tolerant measurements of logical operators in qubit LDPC codes [31, 37, 62–64]. If the logical operation involves two logical fermionic modes, we consider two color code processors. The logical information of the two fermionic modes is individually transferred, logical operations are applied between these two color code blocks, and the information is subsequently returned to memory. Logical operations involving more logical fermionic modes can be performed similarly. For fermionic state transfers between memory and processor, we design a measurement-based circuit as illustrated in Fig. 3(a). This circuit enables the transfer of a single logical fermion information described by logical Majorana operators $\bar{\gamma}_A$ and $\bar{\gamma}'_A$ to a processor described by logical Majorana operators $\bar{\gamma}_B$ and $\bar{\gamma}'_B$, which is initialized in the logical vacuum state $|\bar{0}\rangle_B$. In other words, an output state is the same as the initial state except that the processor logical fermion plays the role of the corresponding logical fermion in memory. During the transfer, a key step is the fault-tolerant measurement of the joint logical operator $i\bar{\gamma}_A \bar{\gamma}_B$, as shown in Fig. 3(a).

We propose two methods for fermionic lattice surgery to realize the fault-tolerant joint measurement, as shown in Fig. 3(b), Fig. 5, and Fig. 6. The first method applies when code B is a fermionic color code with a distance d_B such that $d_B = d_A$, where $d_A = |\bar{\gamma}_A| = |\bar{\gamma}'_A|$

with $|\dots|$ denoting the weight of a Majorana operator string. The second method is applicable when either $d_B = d_A$ or $d_B \neq d_A$, and when code B is either a fermionic color code or a fermionic LDPC code. The procedure proceeds by introducing ancilla Majorana operators between the two codes, modifying the stabilizers associated with $\bar{\gamma}_A$ and $\bar{\gamma}_B$, and adding new stabilizers that merge A and B into a larger fermionic LDPC code $\mathcal{C}_{\text{merged}}$. Since the joint operator $i\bar{\gamma}_A \bar{\gamma}_B$ belongs to the stabilizer group $\mathcal{S}_{\text{merged}}$ of $\mathcal{C}_{\text{merged}}$, it can be measured fault-tolerantly by collecting the outcomes of the stabilizer measurements in $\mathcal{C}_{\text{merged}}$. Figure 3 provides an example of fermionic lattice surgery using method 1. In this example, we align the support of the logical operator $\bar{\gamma}_A$ and $\bar{\gamma}_B$ and introduce a set Q_C of $4(d_A - 1)$ ancilla Majorana operators (corresponding to $2(d_A - 1)$ complex fermion modes) between these two codes, labeled as $\gamma_{a,1}, \gamma'_{a,1}, \dots, \gamma_{a,(d_A-1)}, \gamma'_{a,(d_A-1)}$ and $\gamma_{b,1}, \gamma'_{b,1}, \dots, \gamma_{b,(d_A-1)}, \gamma'_{b,(d_A-1)}$. The original γ -type stabilizer generators at the boundary are modified by including two ancilla Majorana operators. Measurement stabilizer generators M_1, M_2, \dots, M_{d_A} and gauge stabilizer generators $G_1, G_2, \dots, G_{d_A-1}$ are also introduced. The original γ -type stabilizer generators for both block of A and B are not modified. This merging procedure creates a merged stabilizer code $\mathcal{C}_{\text{merged}}$ where $i\bar{\gamma}_A \bar{\gamma}_B$ becomes a stabilizer. In End Matter, we provide guidelines for introducing ancilla Majorana operators and constructing stabilizer generators for both methods. In Supplemental Material, we show that the distance of dressed logical operators is not decreased based on the formalism of the subsystem code [65, 66]. We also show that the number of the Majorana modes introduced during the whole process is small compared to the fermionic LDPC memory, resulting in a small resource overhead.

To achieve the fault-tolerant measurement of $i\bar{\gamma}_A \bar{\gamma}_B$, we first initialize the physical ancilla complex fermions in the $|0\rangle$ state and then measure all the stabilizer generators in the merged code and perform $\min\{d_A, d_B\}$ rounds of error corrections in the presence of noisy measurements to ensure fault-tolerance. Finally, each physical ancilla fermion is measured in the particle number basis to return the state to the original code space.

We now demonstrate the capability of our codes by simulating the quantum circuit of four fermion modes shown in Fig. 4(a). The circuit incorporates tunneling operations that enable the tunneling of fermions between neighboring sites, and onsite measurements, followed by fermionic swap gates, provided the measurement outcome is zero. For an initial state $|0101\rangle$, we expect that the steady state of this dynamical process is a skin state where fermionic particles mainly reside in the upper half part due to feedback effects [67–69]. To simulate the dynamical behavior, we employ the fermionic $[[88, 4, 7]]_f$ double-chain bicycle code as our fermionic LDPC code and use the four logical complex fermion modes without

overlap for the simulation. Additionally, we introduce two copies of the fermionic $[[37, 1, 7]]_f$ color code to function as processors. The calculated time evolution of the particle number at the first and fourth site is shown in Fig. 4(b). The value of $\langle \bar{n}_1 \rangle$ suddenly increases to one while the value of $\langle \bar{n}_4 \rangle$ decreases to zero, which aligns with the expected characteristics of a skin state. Notably, with our fault-tolerant logical operations and error correction techniques, the error-corrected data demonstrate significantly higher fidelity compared to the uncorrected data, as shown in Fig. 4(b).

In summary, we have developed a systematic workflow for constructing fermionic LDPC code memory based on weakly-self-dual CSS codes and proposed methods for executing logical operations based on lattice surgery. We demonstrate that our fermionic LDPC code can be used to simulate dynamics of fermionic systems fault-tolerantly with effective error detection and correction. Such fermion-to-fermion quantum computation has the potential to significantly reduce the computational complexity associated with simulating fermionic systems. Our work encourages the pursuit of high-performance fermionic LDPC codes with higher encoding rates and larger code distances, as well as the advancement of more efficient methods for executing logical operations with reduced overhead.

Note added. During the final stage of this work, we became aware of a related work [70], which uses Majorana LDPC codes to encode logical qubits.

We thank Y. Li, Q. Xu, F. Wei, and Y. Mao for helpful discussions. This work is supported by the National Natural Science Foundation of China (Grant No. 12474265 and No. 11974201) and Innovation Program for Quantum Science and Technology (Grant No. 2021ZD0301604). We also acknowledge the support by center of high performance computing, Tsinghua University.

* These authors contribute equally to this work.

† yongxuphy@tsinghua.edu.cn

- [1] C. W. Bauer, Z. Davoudi, A. B. Balantekin, T. Bhattacharya, M. Carena, W. A. De Jong, P. Draper, A. El-Khadra, N. Gemelke, M. Hanada, *et al.*, *PRX quantum* **4**, 027001 (2023).
- [2] B. Bauer, S. Bravyi, M. Motta, and G. K.-L. Chan, *Chem. Rev.* **120**, 12685 (2020).
- [3] S. McArdle, S. Endo, A. Aspuru-Guzik, S. C. Benjamin, and X. Yuan, *Rev. Mod. Phys.* **92**, 015003 (2020).
- [4] J. Berges, M. P. Heller, A. Mazeliauskas, and R. Venugopalan, *Rev. Mod. Phys.* **93**, 035003 (2021).
- [5] C. M. Varma, *Rev. Mod. Phys.* **92**, 031001 (2020).
- [6] M. Troyer and U.-J. Wiese, *Phys. Rev. Lett.* **94**, 170201 (2005).
- [7] R. P. Feynman, *Int. J. Theor. Phys.* **21**, 467 (1982).
- [8] D. S. Abrams and S. Lloyd, *Phys. Rev. Lett.* **79**, 2586 (1997).
- [9] G. Ortiz, J. E. Gubernatis, E. Knill, and R. Laflamme, *Phys. Rev. A* **64**, 022319 (2001).
- [10] S. B. Bravyi and A. Y. Kitaev, *Ann. Phys.* **298**, 210 (2002).
- [11] R. C. Ball, *Phys. Rev. Lett.* **95**, 176407 (2005).
- [12] F. Verstraete and J. I. Cirac, *J. Stat. Mech.: Theory Exp.* **2005** (09), P09012.
- [13] J. D. Whitfield, V. c. v. Havlíček, and M. Troyer, *Phys. Rev. A* **94**, 030301 (2016).
- [14] D. González-Cuadra, D. Bluvstein, M. Kalinowski, R. Kaubruegger, N. Maskara, P. Naldesi, T. V. Zache, A. M. Kaufman, M. D. Lukin, H. Pichler, *et al.*, *Proc. Natl. Acad. Sci.* **120**, e2304294120 (2023).
- [15] A. Schuckert, E. Crane, A. V. Gorshkov, M. Hafezi, and M. J. Gullans, arXiv:2411.08955 10.48550/arXiv.2411.08955 (2024).
- [16] R. Ott, D. González-Cuadra, T. V. Zache, P. Zoller, A. M. Kaufman, and H. Pichler, *Phys. Rev. Lett.* **135**, 090601 (2025).
- [17] J.-P. Tillich and G. Zémor, *IEEE Transactions on Information Theory* **60**, 1193 (2013).
- [18] D. Gottesman, *Quantum Information and Computation* **14**, 1338 (2013).
- [19] A. A. Kovalev and L. P. Pryadko, *Phys. Rev. A* **88**, 012311 (2013).
- [20] N. P. Breuckmann and B. M. Terhal, *IEEE transactions on Information Theory* **62**, 3731 (2016).
- [21] P. Panteleev and G. Kalachev, *Quantum* **5**, 585 (2021).
- [22] N. P. Breuckmann and J. N. Eberhardt, *IEEE Transactions on Information Theory* **67**, 6653 (2021).
- [23] A. Krishna and D. Poulin, *Phys. Rev. X* **11**, 011023 (2021).
- [24] O. Higgott and N. P. Breuckmann, *Phys. Rev. X* **11**, 031039 (2021).
- [25] N. P. Breuckmann and J. N. Eberhardt, *PRX quantum* **2**, 040101 (2021).
- [26] P. Panteleev and G. Kalachev, *IEEE Transactions on Information Theory* **68**, 213 (2021).
- [27] N. Delfosse, M. E. Beverland, and M. A. Tremblay, arXiv:2109.14599 (2021).
- [28] N. Baspin and A. Krishna, *Quantum* **6**, 711 (2022).
- [29] N. Baspin and A. Krishna, *Phys. Rev. Lett.* **129**, 050505 (2022).
- [30] M. A. Tremblay, N. Delfosse, and M. E. Beverland, *Phys. Rev. Lett.* **129**, 050504 (2022).
- [31] L. Z. Cohen, I. H. Kim, S. D. Bartlett, and B. J. Brown, *Sci. Adv.* **8**, eabn1717 (2022).
- [32] P. Panteleev and G. Kalachev, in *Proceedings of the 54th annual ACM SIGACT symposium on theory of computing* (2022) pp. 375–388.
- [33] A. Leverrier and G. Zémor, in *2022 IEEE 63rd Annual Symposium on Foundations of Computer Science (FOCS)* (IEEE, 2022) pp. 872–883.
- [34] A. Strikis and L. Berent, *PRX Quantum* **4**, 020321 (2023).
- [35] A. O. Quintavalle, P. Webster, and M. Vasmer, *Quantum* **7**, 1153 (2023).
- [36] H.-K. Lin and L. P. Pryadko, *Phys. Rev. A* **109**, 022407 (2024).
- [37] Q. Xu, J. P. Bonilla Ataides, C. A. Pattison, N. Raveendran, D. Bluvstein, J. Wurtz, B. Vasić, M. D. Lukin, L. Jiang, and H. Zhou, *Nat. Phys.* **20**, 1084 (2024).
- [38] S. Bravyi, A. W. Cross, J. M. Gambetta, D. Maslov,

- P. Rall, and T. J. Yoder, *Nature* **627**, 778 (2024).
- [39] G. Zhang and Y. Li, *Phys. Rev. Lett.* **134**, 070602 (2025).
- [40] Y. Li, *Phys. Rev. Res.* **7**, 013115 (2025).
- [41] D. Bluvstein, H. Levine, G. Semeghini, T. T. Wang, S. Ebadi, M. Kalinowski, A. Keesling, N. Maskara, H. Pichler, M. Greiner, *et al.*, *Nature* **604**, 451 (2022).
- [42] D. Bluvstein, S. J. Evered, A. A. Geim, S. H. Li, H. Zhou, T. Manovitz, S. Ebadi, M. Cain, M. Kalinowski, D. Hangleiter, *et al.*, *Nature* **626**, 58 (2024).
- [43] J.-S. Chen, E. Nielsen, M. Ebert, V. Inlek, K. Wright, V. Chaplin, A. Maksymov, E. Pérez, A. Poudel, P. Maunz, *et al.*, *Quantum* **8**, 1516 (2024).
- [44] K. Wang, Z. Lu, C. Zhang, G. Liu, J. Chen, Y. Wang, Y. Wu, S. Xu, X. Zhu, F. Jin, *et al.*, *Nat. Phys.* **22**, 308 (2026).
- [45] D. J. C. MacKay, G. Mitchison, and P. L. McFadden, *IEEE Transactions on Information Theory* **50**, 2315 (2004).
- [46] D. Cao, Y. L. Song, and S. M. Zhao, *J. Electronics* **29**, 1 (2012).
- [47] S. A. Aly, in *IEEE GLOBECOM 2008-2008 IEEE Global Telecommunications Conference* (IEEE, 2008) pp. 1–5.
- [48] J. Farinholt, *arXiv:1207.0732* (2012).
- [49] Z.-C. Liu, C.-Y. Xu, and Y. Xu, *Self-dual stacked quantum low-density parity-check codes* (2026), *arXiv:2602.15372*.
- [50] A. Kitaev, *Ann. Phys.* **321**, 2 (2006).
- [51] S. Bravyi, B. M. Terhal, and B. Leemhuis, *New J. Phys.* **12**, 083039 (2010).
- [52] M. A. Nielsen and I. L. Chuang, *Quantum computation and quantum information* (Cambridge university press, 2010).
- [53] H. Bombin and M. A. Martin-Delgado, *J. Math. Phys.* **48**, 052105 (2007).
- [54] L. Aghababaie Beni, O. Higgott, and N. Shutty, *Tesseract: A search-based decoder for quantum error correction* (2025), *arXiv:2503.10988*.
- [55] J. Liang, Q. Wang, L. Li, L. Song, and X. Ma, *The European Physical Journal Special Topics* , 1 (2025).
- [56] J. Roffe, D. R. White, S. Burton, and E. Campbell, *Phys. Rev. Res.* **2**, 043423 (2020).
- [57] D. Litinski and F. von Oppen, *Phys. Rev. B* **97**, 205404 (2018).
- [58] S. Vijay, T. H. Hsieh, and L. Fu, *Phys. Rev. X* **5**, 041038 (2015).
- [59] C. McLauchlan and B. Béri, *Quantum* **8**, 1400 (2024).
- [60] Y. Prasetia, R. Kurnia, A. Andriko, and P. Astuti, *International Electronic Journal of Algebra* , 1 (2025).
- [61] B. Vasic, V. Savin, M. Pacenti, S. Borah, and N. Raveendran, *arXiv preprint arXiv:2510.14090* (2025).
- [62] D. Horsman, A. G. Fowler, S. Devitt, and R. Van Meter, *New J. Phys.* **14**, 123011 (2012).
- [63] A. G. Fowler and C. Gidney, *arXiv:1808.06709* (2018).
- [64] H. Poulsen Nautrup, N. Friis, and H. J. Briegel, *Nat. Commun.* **8**, 1321 (2017).
- [65] C. Vuillot, L. Lao, B. Criger, C. G. Almudéver, K. Bertels, and B. M. Terhal, *New J. Phys.* **21**, 033028 (2019).
- [66] S. A. Aly, A. Klappenecker, and P. K. Sarvepalli, *arXiv preprint quant-ph/0610153* (2006).
- [67] Y.-P. Wang, C. Fang, and J. Ren, *Phys. Rev. B* **110**, 035113 (2024).
- [68] X. Feng, S. Liu, S. Chen, and W. Guo, *Phys. Rev. B* **107**, 094309 (2023).
- [69] Z.-C. Liu, K. Li, and Y. Xu, *Phys. Rev. Lett.* **133**, 090401 (2024).
- [70] M. Mudassar, A. Schuckert, and D. Gottesman, *arXiv:2508.09928* (2025).
- [71] L. Storme, in *Handbook of combinatorial designs* (Chapman and Hall/CRC, 2006) pp. 728–754.
- [72] A. A. Albert and R. Sandler, *An introduction to finite projective planes* (Courier Corporation, 2015).
- [73] J. Roffe, *Contemporary Physics* **60**, 226 (2019).
- [74] T. Tansuwannont, Y. Takada, and K. Fujii, *arXiv preprint arXiv:2503.19790* (2025).
- [75] J. L. Gross, J. Yellen, and M. Anderson, *Graph theory and its applications* (Chapman and Hall/CRC, 2018).
- [76] A. G. Fowler, A. M. Stephens, and P. Groszkowski, *Physical Review A* **80**, 052312 (2009).
- [77] J. Roffe, *LDPC: Python tools for low density parity check codes* (2022).
- [78] C. Gidney, *Quantum* **5**, 497 (2021).

End Matter

In the End Matter, we will provide the guidelines for introducing ancilla Majorana operators and constructing stabilizer generators for fermionic lattice surgery.

For clarity, we use the following terminology: additional Majorana operators are termed ancilla Majorana operators, stabilizers inherited from the original codes and modified during the merging are called modified stabilizers, newly introduced stabilizers acting solely on ancilla Majorana operators are termed gauge stabilizers, and stabilizers involving Majorana operators from both codes A and B are referred to as measurement stabilizers.

Method 1.—Since logical operators in our fermionic LDPC code all have odd weight, for any $\bar{\gamma}_A$ in a fermionic LDPC code memory A , we can always select a triangular color code B [15, 51] encoding a single pair of logicals $(\bar{\gamma}_B, \bar{\gamma}'_B)$, with $|\bar{\gamma}_A| = |\bar{\gamma}_B| = |\bar{\gamma}'_B| = d$. Method 1 as detailed in the following is applicable to the lattice surgery

between a fermionic LDPC code and a fermionic color code with $|\bar{\gamma}_A| = |\bar{\gamma}_B|$.

We align the support of $\bar{\gamma}_A$ and $\bar{\gamma}_B$ in a pair of parallel lines, each consisting of d points, as shown in Fig. 3(b), and indexing them as $\{\gamma_{A,i}\}_{i=1}^d$ and $\{\gamma_{B,i}\}_{i=1}^d$ from left to right, respectively. We also index the checks supported on A (B) that are associated with $\bar{\gamma}_A$ ($\bar{\gamma}_B$) as $\{c_{A,i}\}_{i=1}^{N_A}$ ($\{c_{B,i}\}_{i=1}^{N_B}$), where N_A and $N_B = d - 1$ are the number of stabilizers associated with $\bar{\gamma}_A$ and $\bar{\gamma}_B$, respectively. As shown in Fig. 5, each c_B forms a plaquette on the boundary of the color code lattice. We now introduce ancilla Majorana modes, modify the original stabilizers, and introduce new stabilizers step by step.

We first modify all the stabilizers $c_{A,i}$ and $c_{B,i}$ by introducing ancilla Majorana operators. Specifically, consider

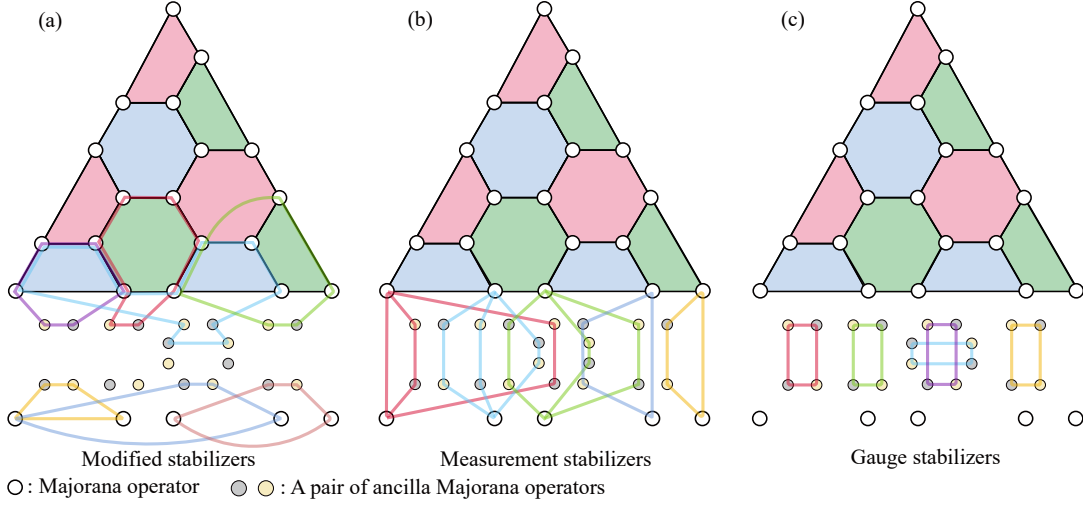


FIG. 5. Illustration of modified stabilizers in (a), measurement stabilizers in (b), and gauges stabilizers in (c) for a specific case of fermionic lattice surgery using method 1. Before merging, the original stabilizers include those of the fermionic LDPC code, the color code, and the stabilizers of ancilla Majorana operators (each stabilizer includes a pair of ancilla Majorana operators forming a complex fermion).

each

$$(c_{A,i})_{\bar{A}} \sim \gamma_{A,j_1} \gamma_{A,j_2} \cdots \gamma_{A,j_{m_i}}, \quad (2)$$

where $1 \leq j_1 < \cdots < j_{m_i} \leq d$, \sim denotes equality up to a phase, \bar{A} denotes the support of $\bar{\gamma}_A$, $(\cdots)_{\bar{A}}$ is the operator constrained on \bar{A} , and $m_i = |(c_{A,i})_{\bar{A}}|$ is an even number, ensured by the commutativity between $\bar{\gamma}_A$ and $c_{A,i}$. We introduce m_i ancilla Majorana operators $\{\gamma_{a,i,j_1}, \gamma'_{a,i,j_2}, \cdots, \gamma_{a,i,j_{m_i-1}}, \gamma'_{a,i,j_{m_i}}\}$, where the subscript a indicates that these modes are associated with the stabilizer of A , i is the index of the stabilizer $c_{A,i}$, and j_1, j_2, \dots, j_{m_i} correspond to the positions of the Majorana operators in $c_{A,i}$ in the support of $\bar{\gamma}_A$. The last two subscripts are used to index the order of the ancilla modes, corresponding to the second subscript in $\gamma_{a,j}$ and $\gamma'_{a,j}$ with $1 \leq j \leq d_A - 1$ as described in the main text. We modify the stabilizer $c_{A,i}$ to

$$c'_{A,i} \sim c_{A,i} \gamma_{a,i,j_1} \gamma'_{a,i,j_2} \cdots \gamma_{a,i,j_{m_i-1}} \gamma'_{a,i,j_{m_i}}. \quad (3)$$

Similarly, we introduce m_i ancilla Majorana operators $\{\gamma_{b,i,j_1}, \gamma'_{b,i,j_2}, \cdots, \gamma_{b,i,j_{m_i-1}}, \gamma'_{b,i,j_{m_i}}\}$ for code B . For each pair $(\gamma_{a,i,j_{2n-1}}, \gamma'_{a,i,j_{2n}})$ with $1 \leq n \leq m_i/2$:

- If $j_{2n-1} + 1 = j_{2n}$, we introduce a modified stabilizer in code B as $c'_{B,i} \sim c_{B,i} \gamma_{b,i,j_{2n-1}} \gamma'_{b,i,j_{2n}}$, and a gauge stabilizer as $\gamma_{a,i,j_{2n-1}} \gamma'_{a,i,j_{2n}} \gamma_{b,i,j_{2n-1}} \gamma'_{b,i,j_{2n}}$.
- If $j_{2n-1} + 2 = j_{2n}$, this modified stabilizer is defined as $c'_{B,i} \sim c_{B,j_{2n-1}} c_{B,j_{2n-1}} \gamma_{b,i,j_{2n-1}} \gamma'_{b,i,j_{2n}}$, and the gauge stabilizer is $\gamma_{a,i,j_{2n-1}} \gamma'_{a,i,j_{2n}} \gamma_{b,i,j_{2n-1}} \gamma'_{b,i,j_{2n}}$.
- Otherwise, we add 4 additional Majorana modes $\{\gamma_{b,i,j_{2n-1}+1}, \gamma'_{b,i,j_{2n}-1}, \gamma_{a,i,j_{2n-1}+1}, \gamma'_{a,i,j_{2n}-1}\}$,

let the modified stabilizer be $c'_{B,i} \sim c_{B,j_{2n-1}} c_{B,j_{2n-1}} \gamma_{b,i,j_{2n-1}} \gamma'_{b,i,j_{2n-1}+1} \gamma_{b,i,j_{2n-1}} \gamma'_{b,i,j_{2n}}$, and introduce two gauge stabilizers as $\gamma_{a,i,j_{2n-1}} \gamma'_{a,i,j_{2n}} \gamma_{b,i,j_{2n-1}} \gamma'_{b,i,j_{2n}}$, $\gamma_{a,i,j_{2n-1}+1} \gamma'_{a,i,j_{2n}-1} \gamma_{b,i,j_{2n-1}+1} \gamma'_{b,i,j_{2n}-1}$.

We repeat this process for each $c_{A,i}$. We note that for those unused $c_{B,i}$ after iterating over all $c_{A,i}$, say the number of which as M_B . For each such $c_{B,m}$, where $1 \leq m \leq M_B$ represents the index of $c_{B,m}$, we further introduce four Majorana operators $\{\gamma_{b,N_A+m,i}, \gamma'_{b,N_A+m,i+1}, \gamma_{a,N_A+m,i}, \gamma'_{a,N_A+m,i+1}\}$, define a modified stabilizer $c'_{B,i}$ as $c_{B,i} \gamma_{b,N_A+m,i} \gamma'_{b,N_A+m,i+1}$, and add a gauge stabilizer as $\gamma_{b,N_A+m,i} \gamma'_{b,N_A+m,i+1} \gamma_{a,N_A+m,i} \gamma'_{a,N_A+m,i+1}$.

After that, we define d measurement stabilizers $\{M_i\}_{i=1}^d$ as

$$M_i \sim \gamma_{A,i} \gamma_{B,i} \prod_n^{(i)} \gamma_{a,n,i} \gamma_{b,n,i}^{(i)}, \quad (4)$$

where $\prod_n^{(i)} \gamma_{a,n,i} \gamma_{b,n,i}^{(i)}$ denotes the product of all ancilla Majorana operator (either of γ -type or γ' -type) at site i with n running over the subscripts of the ancilla modes associated with $\gamma_{A,i}$ and $\gamma_{B,i}$. In other words, the measurement stabilizer at site i consists of $\gamma_{A,i}$, $\gamma_{B,i}$ and all ancilla Majorana operators at this position. We note that $i\bar{\gamma}_A \bar{\gamma}_B$ is proportional to the product of all measurement stabilizers and the gauge stabilizers, since all $\gamma_{A,i}$ and $\gamma_{B,i}$ appear once and all ancilla Majorana operators appear twice in this product and thus cancel out. Figure 5 displays all modified, measurement, and gauge stabilizers for an illustrative case, which is more complicated than that in Fig. 3(b).

Method 2.—We now introduce the second method for fermionic lattice surgery applicable when $|\bar{\gamma}_A| = |\bar{\gamma}_B|$ or $|\bar{\gamma}_A| \neq |\bar{\gamma}_B|$, and when code B is either a fermionic color code or a fermionic LDPC code (see Supplemental Material for Pseudo-code). As an example depicted in Fig. 6(a), we align a weight-5 logical operator $\bar{\gamma}_A$ of fermionic LDPC code A and a weight-3 logical operator $\bar{\gamma}_B$ of fermionic color code B in two parallel lines, and index the Majorana modes in these two lines from top to bottom as $\{\gamma_{A,i}\}_{i=1}^5$ and $\{\gamma_{B,i}\}_{i=1}^3$, respectively.

We first modify the original stabilizers associated with $\bar{\gamma}_A$ and $\bar{\gamma}_B$. As shown in Fig. 6(a), there are $N_A = 4$ stabilizers for $\bar{\gamma}_A$ and $N_B = 2$ stabilizers for $\bar{\gamma}_B$, whose weights of overlap with $\bar{\gamma}_A$ and $\bar{\gamma}_B$ are denoted as $\{m_{A,i}\}_{i=1}^{N_A}$ and $\{m_{B,i}\}_{i=1}^{N_B}$, respectively. For each stabilizer $c_{A,i}$ and $c_{B,i}$, we introduce $m_{A,i}$ and $m_{B,i}$ ancilla Majorana operators $\{\gamma_{a,i,j_1}, \gamma'_{a,i,j_2}, \dots, \gamma_{a,i,j_{m_{A,i}-1}}, \gamma'_{a,i,j_{m_{A,i}}}\}$ and $\{\gamma_{b,i,j_1}, \gamma'_{b,i,j_2}, \dots, \gamma_{b,i,j_{m_{B,i}-1}}, \gamma'_{b,i,j_{m_{B,i}}}\}$, respectively, where j_k correspond to the vertical positions of the Majorana operators in $c_{A,i}$ or $c_{B,i}$. We modify $c_{A(B),i}$ to $c'_{A(B),i}$ by multiplying these ancilla Majorana operators as before, as shown in Fig. 6(b). The difference is that, in this case, the modified stabilizer $c'_{B,i}$ is constructed from a single stabilizer $c_{B,i}$, instead of the product of several stabilizers in the previous case.

Next, we define the measurement stabilizers $\{M_i\}_{i=1}^{D_{AB}}$,

where $D_{AB} = (|\bar{\gamma}_A| + |\bar{\gamma}_B|)/2$. For the first $\min\{|\bar{\gamma}_A|, |\bar{\gamma}_B|\}$ measurement stabilizer M_i , we define M_i as the product of $\gamma_{A,i}$, $\gamma_{B,i}$, and all ancilla Majorana modes at site i , that is,

$$M_i \sim \gamma_{A,i} \gamma_{B,i} \prod_{n_a, n_b} \gamma_{a, n_a, i}^{(\prime)} \gamma_{b, n_b, i}^{(\prime)}, \quad (5)$$

where $\prod_{n_a, n_b} \gamma_{a, n_a, i}^{(\prime)} \gamma_{b, n_b, i}^{(\prime)}$ denotes the product of all ancilla Majorana operators at site i (either of γ -type or γ' -type) with n_a and n_b running over the subscripts of the ancilla modes associated with $\gamma_{A,i}$ and $\gamma_{B,i}$, respectively. For the remaining $(|\bar{\gamma}_A| - |\bar{\gamma}_B|)/2$ measurement stabilizers $\{M_i\}_{i=\min\{|\bar{\gamma}_A|, |\bar{\gamma}_B|\}+1}^{D_{AB}}$, they are defined as the product of a pair of Majorana operators in $\{\gamma_{A,i}\}$ or $\{\gamma_{B,i}\}$, and the ancilla Majorana modes associated with them. For example, in Fig. 6(c), we define $M_4 \sim \gamma_{A,4} \gamma_{A,5} \gamma'_{a,1,4} \gamma'_{a,3,4} \gamma'_{a,4,5}$. We note that if any M_i has odd weight, we introduce an additional ancilla mode $\gamma_{p,i}$, and modify M_i to $M_i \gamma_{p,i}$ up to a phase factor to ensure even weight, as shown in the first and fourth measurement stabilizers in Fig. 6(c). The number of such additional ancilla modes is denoted as N_P , which must be even since the product of all measurement stabilizers is an even-weight operator. Gauge stabilizers are then identified from a graph theory perspective, as detailed in Supplemental Material.

In the Supplemental Material, we will review Majorana stabilizer codes and detail our method for identifying odd-weight logical operators in a fermionic LDPC code in Section S-1, validate the quantum state teleportation circuit in Section S-2, analyze the overhead of fermionic lattice surgery and prove the fault-tolerance of this procedure in Section S-3, and finally provide more details regarding calculations of the logical failure rate of the fermionic LDPC memory and simulations of fermionic circuits in Section S-4.

S-1. CONSTRUCTION OF FERMIONIC LDPC CODES

In this section, we will follow Ref. [51] to review Majorana stabilizer codes and detail our method for identifying odd-weight logical operators in a fermionic LDPC code.

A. Majorana stabilizer codes

In this subsection, we will review the Majorana stabilizer codes (also see Ref. [51]). Consider the group of Majorana operators, $\text{Maj}(2n) \equiv \left\{ \Gamma = \eta \prod_{j=1}^n \gamma_j^{\alpha_j} (\gamma'_j)^{\alpha'_j} \mid \alpha_j, \alpha'_j \in \{0, 1\}, \eta \in \{\pm 1, \pm i\} \right\}$, where γ_j and γ'_j with $j = 1, \dots, n$ are Majorana operators satisfying $\{\gamma_i, \gamma_j\} = 2\delta_{ij}$, $\{\gamma'_i, \gamma'_j\} = 2\delta_{ij}$, $\{\gamma_i, \gamma'_j\} = 0$. These Majorana operators arise from complex fermion's creation (denoted c_j^\dagger) and annihilation operators (denoted c_j) via $\gamma_j = c_j + c_j^\dagger$ and $\gamma'_j = i(c_j - c_j^\dagger)$. Analogous to Pauli stabilizer codes being defined based on the Pauli group [52], Majorana stabilizer codes are defined based on the group of Majorana operators [51].

To handle the group multiplication structure more systematically, we consider a $2n$ -dimensional vector space \mathbb{F}_2^{2n} , where \mathbb{F}_2 is the binary field $\{0, 1\}$. We then construct an isomorphism $\phi: \text{Maj}(2n) \rightarrow \mathbb{F}_2^{2n} \otimes \{\pm 1, \pm i\}$, mapping each element Γ to a binary vector $\vec{\gamma} \in \mathbb{F}_2^{2n}$ and a phase η ,

$$\phi(\Gamma) = (\vec{\gamma}, \eta) \quad \text{where} \quad \vec{\gamma} = (\alpha_1, \alpha'_1, \alpha_2, \alpha'_2, \dots, \alpha_n, \alpha'_n)^T. \quad (S1)$$

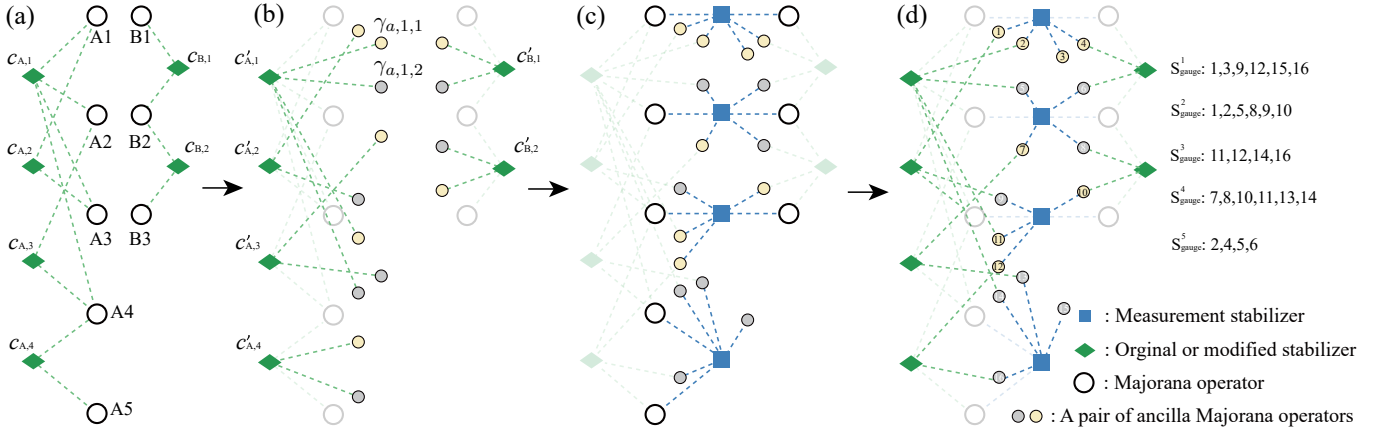


FIG. 6. Illustration of how to add ancilla Majorana modes and stabilizers for a merged code using method 2. Here we consider two logical operators in codes A and B, supported by five and three Majorana operators, respectively. Initially, we have two logical operators described by the original stabilizer generators represented by green rhombuses and Majorana operators represented by circles for code A in the support of $\bar{\gamma}_A$ and for code B in the support of $\bar{\gamma}_B$ (see (a)). Pairs of ancilla Majorana operators (yellow and gray circles) are added following the rules detailed in the text, and the modified stabilizer generators are introduced (see (b)). We then incorporate measurement stabilizer generators with an additional pair of ancilla Majorana operators to make their weights even (see (c)). In (d), we label all ancilla modes and construct a graph with vertices corresponding to stabilizers and ancilla Majorana modes, and edges defined between them accordingly, which corresponds to Fig. S3(a) in Supplemental Material. The gauge stabilizer generators are also presented in Fig. S3(c) in Supplemental Material.

To ensure that $\text{Maj}(2n) \cong \mathbb{F}_2^{2n} \times \{\pm 1, \pm i\}$, we define $(\vec{\gamma}_1, \eta_1) \cdot (\vec{\gamma}_2, \eta_2) \equiv (\vec{\gamma}_1 \oplus \vec{\gamma}_2, \eta_1 \eta_2 f(\vec{\gamma}_1, \vec{\gamma}_2))$, where $\vec{\gamma}_1 \oplus \vec{\gamma}_2$ is the standard component-wise addition modulo 2 on \mathbb{F}_2^{2n} , equivalent to the XOR operation, and the factor $f(\vec{\gamma}_1, \vec{\gamma}_2) \in \{1, -1\}$, termed the sign function, encodes a sign arising from the inherent anticommutation relations of the Majorana operators. Based on a common operator ordering convention, we define the sign function as $f \equiv (-1)^{\sum_k [\vec{\gamma}_2]_k m_k}$, where m_k counts the number of nonzero elements in $\{[\vec{\gamma}_1]_k, [\vec{\gamma}_1]_{k+1}, \dots, [\vec{\gamma}_1]_{2n}\}$.

For any elements $\Gamma_1, \Gamma_2 \in \text{Maj}(2n)$, they either commute or anticommute. Specifically, we have $\Gamma_1 \Gamma_2 = \Gamma_2 \Gamma_1 (-1)^{p(\vec{\gamma}_1)p(\vec{\gamma}_2) \oplus \vec{\gamma}_1 \cdot \vec{\gamma}_2}$ [51], where $\vec{\gamma}_j$ represents the vector mapped from Γ_j , and $p(\vec{\gamma})$ is a parity function denoting the parity of the number of nonzero entries in the vector $\vec{\gamma}$: 0 indicates an even parity and 1 indicates an odd parity. We see that two even-weight Majorana strings commute if their overlap has even weight and anticommute if their overlap has odd weight. One thus can encode logical Majorana operators as even-weight physical Majorana operator strings. However, if two logical Majorana operators are located in different blocks, which have no overlap, then odd-weight strings must be considered, as they anticommute with each other.

The Majorana stabilizer code is defined by a Majorana stabilizer group $\mathcal{S}_{\text{maj}} = \langle g_1, \dots, g_m \rangle$ generated by independent Majorana operator strings $g_j \in \text{Maj}(2n)$ with $j = 1, \dots, m$. Each element in the group commutes with any other elements in it. The code space \mathbb{H}_L is a subspace spanned by all state vectors that are simultaneous eigenstates of all stabilizer operators corresponding to eigenvalue +1 [52]. The check matrix is defined as

$$H = \begin{pmatrix} \vec{g}_1^T \\ \vdots \\ \vec{g}_m^T \end{pmatrix}, \quad (\text{S2})$$

where the vector \vec{g}_j with $j = 1, \dots, m$ corresponds to a stabilizer generator g_j . To preserve the parity of a physical fermion system, we suppose that all stabilizers have even weight. In this case, H is a parity-check matrix of a self-orthogonal linear code, satisfying $HH^T = 0$. Logical operators correspond to operators that commute with all stabilizers but are not in the stabilizer group. Mathematically, a set of all logical operators $\mathcal{L} = \mathcal{C}(\mathcal{S}) \setminus \mathcal{S}$, where $\mathcal{C}(\mathcal{S})$ denotes the centralizer whose elements commute with all elements in \mathcal{S} . The code distance is determined by the minimum weight in \mathcal{L} .

We can use weakly-self-dual CSS codes on qubits to construct Majorana stabilizer codes [15, 51]. Let A be the parity-check matrix of a weakly-self-dual CSS code with parameters $[[n, k, d]]$, satisfying $AA^T = 0$ [45]. We write $A = (\vec{u}_1, \vec{u}_2, \dots, \vec{u}_{m/2})^T$, where m is an even positive integer, and suppose that the row vectors in A are linearly independent, corresponding to stabilizer generators. Consequently, $\{\vec{u}_1, \vec{u}_2, \dots, \vec{u}_{m/2}, \vec{\gamma}_1, \dots, \vec{\gamma}_k\}$ forms a basis for $\ker(A)$ with $\{\vec{\gamma}_j \mid j = 1, \dots, k\}$ corresponding to independent logical operators. The set of logical operators is expressed as $L =$

$\{\sum_{j=1}^{m/2} a_j \vec{u}_j + \sum_{j=1}^k b_j \vec{\gamma}_j \mid a_j, b_j \in \{0, 1\} \text{ and } (b_1, b_2, \dots, b_k)^T \neq \vec{0}\}$ with each vector contributing an X and a Z logical operator. The code distance is thus determined by the minimum weight of the vectors in L . We now use the direct sum $H = A \oplus A$ to form a Majorana stabilizer code's check matrix for n complex fermion modes. The code can be represented by a Tanner graph which has mirror reflection symmetry, where the blue and green squares correspond to γ -type stabilizers and γ' -type stabilizers, respectively, as shown in Fig. S1(a). The set L also describes all logical operators in the Majorana stabilizer code. However, for the fermionic LDPC codes, we aim to find odd-weight logical operators with even overlap. We examine fermionic finite projective geometry codes, fermionic finite Euclidean geometry codes, fermionic bicycle codes, and fermionic stacked LDPC codes, finding that these codes considered have $2k$ odd-weight logical operators with even overlap. In other words, the vectors $\vec{\gamma}_1, \dots, \vec{\gamma}_k$ all have odd weight and even overlap (see Table I). This finding indicates that these fermionic LDPC codes can encode k logical complex fermion modes. Thus, the code distance remains determined by the minimum weight of the vectors in L . To sum up, these fermionic LDPC codes maintain the same code parameters $[[n, k, d]]_f$ as the original qubit codes.

B. Examples of weakly-self-dual CSS codes

In this subsection, we will review four types of weakly-self-dual CSS codes: Kitaev Majorana code [50], bicycle code [45] (Fig. S1(b)), Euclidean geometry codes on finite fields [46, 47] (Fig. S1(c)), and projective geometry codes on finite fields [48] (Fig. S1(d)). Very recently, we provide a method to construct weakly-self-dual CSS codes based on a CSS code that may not be weakly self dual (see Ref. [49]).

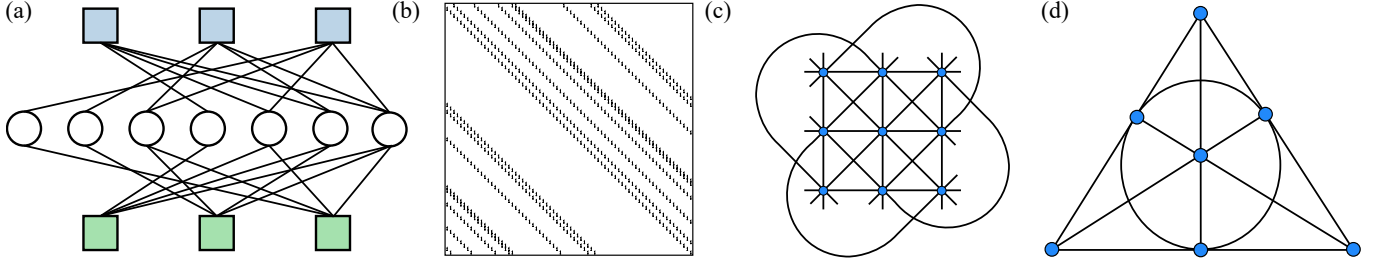


FIG. S1. (a) The Tanner graph description of the Steane code. The circles, blue and green squares represent the fermions, the γ -type stabilizers, and the γ' -type stabilizers, respectively. (b) Illustration of a circulant matrix used to construct bicycle codes. (c) Illustration of the Euclidean geometry when $(m, q) = (2, 3)$. In this special case, the lines are the straight lines on a torus with different directions. (d) The Fano plane, which is the simplest example of a finite projective plane. We will use many planes like this in code construction from finite projective geometry.

Kitaev Majorana code

According to Ref. [50], any $[[n, k, d]]$ qubit stabilizer code defined by a qubit stabilizer group \mathcal{S} can be mapped to a $[[2n, k, 2d]]_f$ Majorana stabilizer code defined by \mathcal{S}_{maj} . For each qubit j , four Majorana operators $\gamma_j^g, \gamma_j^{x,y,z}$ are introduced so that the Majorana stabilizer code is defined by $4n$ Majorana operators. The Pauli operators of each qubit j in the generators of \mathcal{S} are mapped to the product of these Majorana operators by

$$\begin{cases} \sigma_j^x \rightarrow i\gamma_j^x \gamma_j^g \\ \sigma_j^y \rightarrow i\gamma_j^y \gamma_j^g \\ \sigma_j^z \rightarrow i\gamma_j^z \gamma_j^g \end{cases}, \quad (\text{S3})$$

forming generators in \mathcal{S}_{maj} . In addition, n gauge stabilizers $G_j = \gamma_j^x \gamma_j^y \gamma_j^z \gamma_j^g$ are added into \mathcal{S}_{maj} . The k logical operators of the Majorana stabilizer code are given by replacing the Pauli operators in the original qubit code with the Majorana modes. Specifically, consider a $[[n, k, d]]$ qubit CSS code with an X check matrix H_X and Z check matrix H_Z satisfying $H_X H_Z^T = 0$. The corresponding Majorana stabilizer code has the check matrix

$$H = \begin{pmatrix} H_X & H_X & 0 & 0 \\ H_Z & 0 & 0 & H_Z \\ I_n & I_n & I_n & I_n \end{pmatrix}, \quad (\text{S4})$$

where I_n is an $n \times n$ identity matrix. In this case, the group of Majorana operators reads $\text{Maj}(2n) \equiv \{\Gamma = \eta \prod_{j=1}^n (\gamma_j^x)^{\alpha_{j,1}} (\gamma_j^y)^{\alpha_{j,2}} (\gamma_j^z)^{\alpha_{j,3}} (\gamma_j^i)^{\alpha_{j,4}} | \alpha_{j,1}, \alpha_{j,2}, \alpha_{j,3}, \alpha_{j,4} \in \{0, 1\}, \eta \in \{\pm 1, \pm i\}\}$. The exponent factors of a Majorana stabilizer generator in $\text{Maj}(2n)$ correspond to each row in H . Since there exists a stabilizer corresponding to a vector of $(1, 1, \dots, 1)$, all logical operators must have even weight so as to commute with this stabilizer. In other words, one cannot find odd-weight logical operators in the Kitaev Majorana stabilizer code.

Finite Euclidean geometry codes

In 2008, Aly proposed a class of self-dual qubit CSS codes based on the incidence matrix of finite Euclidean geometry [47]. However, we find that Aly's finite Euclidean geometry codes fail to produce odd-weight logical Majorana operators. We adopt the revised version of finite Euclidean geometry codes proposed by Cao et al. in Ref. [46] to construct our fermionic LDPC code that contains odd-weight logical Majorana operators.

Here, we will follow Ref. [46] to briefly review the generalized finite Euclidean geometry code. For positive integers (m, q) , a Euclidean geometry $\text{EG}(m, q)$ consists of q^m points, each represented by an m -tuple. Here, m denotes the spatial dimension, while q represents the number of points per dimension. As shown in Fig. S1(c), $\text{EG}(2, 3)$ has two dimensions with three points per dimension, forming the Euclidean space through their Cartesian product. Consider $q = p^s$ for some prime p and positive integer s , with tuple elements drawn from the Galois field \mathbb{F}_q . First, we describe point representation before defining lines. For any prime p and positive integer s , there exists α satisfying $\alpha^{p^s} - \alpha = 0$, where $\mathbb{F}_{p^s} = \{0, 1, \alpha, \alpha^2, \dots, \alpha^{p^s-2}\}$ [71]. For any positive integer m , \mathbb{F}_{q^m} constitutes an extension field over \mathbb{F}_q , with elements expressible as $e = a_0 + a_1\alpha + \dots + a_{m-1}\alpha^{m-1}$ ($a_i \in \mathbb{F}_q$). As illustrated in Fig. S1(c), each line in $\text{EG}(2, 3)$ contains exactly three points. Thus, a bijection exists between \mathbb{F}_{q^m} and m -tuples in $\text{EG}(m, q)$. A line in $\text{EG}(m, q)$ (or \mathbb{F}_{q^m}) is defined as the set containing exactly q points: $\{e_j + \beta e_k | \beta \in \mathbb{F}_q\}$, where $e_j, e_k \in \mathbb{F}_{q^m}$ and $e_k \neq 0$ [71]. We now enumerate and classify these lines. There are q^m choices for e_j and $q^m - 1$ for e_k . Since each line contains exactly q points, q distinct e_k choices yield identical lines. Additionally, $\{e_j + \alpha\beta e_k\}$ with $\beta \in \mathbb{F}_q \setminus \{0\}$ produces identical line sets. Consequently, the total number of lines is $\frac{q^m(q^m-1)}{q(q-1)}$, while the number of lines excluding the origin point is $\frac{(q^{m-1}-1)(q^m-1)}{q-1}$ [46, 71].

For a line $L = \{e_{l_0}, e_{l_1}, \dots, e_{l_{q-1}}\}$, translation via multiplication by a nonzero $e \in \mathbb{F}_{q^m}$ yields $eL = \{ee_{l_0}, ee_{l_1}, \dots, ee_{l_{q-1}}\}$. The $q^m - 1$ lines $\{L, eL, e^2L, \dots, e^{q^m-2}L\}$ form an equivalence class. There exist $J = \frac{q^m-1}{q-1}$ such equivalence classes [47]. $J(q^m - 1) \times (q^m - 1)$ binary check matrices H_j ($1 \leq j \leq J$) are then constructed with rows corresponding to lines in the j -th equivalence class (each row is a binary vector indicating inclusion of points from the origin-excluding line) [46]. The full check matrix is then defined as

$$H_X = H_Z = (H_1^T, \dots, H_J^T, H_1, \dots, H_J). \quad (\text{S5})$$

Since H_j with $j = 1, \dots, J$ are cyclic matrices, H_X satisfies $H_X H_X^T = 0$ and thus gives rise to a self-dual CSS code.

Finite projective plane code

The finite projective plane code is a class of self-dual CSS codes constructed by Farinholt, with the help of the finite projective plane [72]. A projective plane $\text{PG}(2, q)$ with $q = 2^s$ consists of a set of points and lines that satisfy:

1. Any two distinct points determine a unique line;
2. Any two distinct lines intersect at a unique point;
3. There exist four points, no three of which are collinear;
4. Each line contains $q + 1$ points;
5. Each point lies on $q + 1$ lines;
6. There are exactly $q^2 + q + 1$ points and lines [72].

We depict $\text{PG}(2, 2)$ as an example in Fig. S1(d). The points can be represented by the equivalence classes of $[x, y, z] \equiv \{[cx, cy, cz] | [x, y, z] \neq [0, 0, 0], c \in \mathbb{F} \setminus \{0\}\}$. We note that there are $(q^3 - 1)/(q - 1) = q^2 + q + 1$ such equivalence classes, which correspond to the points in the projective plane. The lines can be represented by the equivalence

classes $(a, b, c) \equiv \{(\lambda a, \lambda b, \lambda c) | (a, b, c) \neq [0, 0, 0], \lambda \in \mathbb{F} \setminus \{0\}\}$, such that $ax + by + cz = 0$. Each line contains $q + 1$ points, and there are $q^2 + q + 1$ such lines.

The incidence matrix of the projective plane is a binary matrix B with its entry $B_{i,j} = 1$ if point i lies on line j , and 0 otherwise. Specifically, we only use a subset of lines and points (i.e., skew lines and non-hyperoval points [48]) to construct matrix B . The check matrix of this self-dual CSS code is then defined as

$$H_X = H_Z = (B \ \mathbf{1}), \quad (\text{S6})$$

where $\mathbf{1}$ is a column vector of ones. We note that $HH^T = BB^T + \mathbf{1}\mathbf{1}^T = 0$, because the overlap between any two rows of B is odd ($q + 1$ or 1), and thus BB^T is a $\frac{q^2-q}{2} \times \frac{q^2-q}{2}$ binary matrix with all entries being one.

Bicycle code

In 2004, Mackay et al. proposed a so-called bicycle code in Ref. [45], which is a self-dual CSS code with two check matrices H_X and H_Z that satisfy $H_X = H_Z$ and $H_X H_X^T = 0$, thereby enabling the construction of Majorana LDPC codes. The check matrix of the bicycle code on $2n$ qubits is defined by

$$H_X = H_Z = [C, C^T], \quad (\text{S7})$$

where C is an $n \times n$ cyclic matrix; each row of a cyclic matrix is obtained by right-cyclic shifting of the previous row, as illustrated in Fig. S1(b). Formally, let S be an $n \times n$ matrix defined by $S_{i,j} = 1$ ($1 \leq i, j \leq n$) if $j = (i + 1) \bmod n$ and $S_{i,j} = 0$ otherwise, which reads

$$S = \begin{pmatrix} 0 & 1 & 0 & \dots & 0 \\ 0 & 0 & 1 & \dots & 0 \\ \vdots & \vdots & \vdots & \dots & 0 \\ 0 & 0 & 0 & \dots & 1 \\ 1 & 0 & 0 & \dots & 0 \end{pmatrix}. \quad (\text{S8})$$

The cyclic matrix C with weight r is defined by $C = \sum_{i=1}^r S^{a_i}$, where $1 \leq a_i \leq n$. The code is a self-dual CSS code since $H_X H_X^T = CC^T + C^T C = 0$.

As a demonstration, we construct a $[[100, 20, 7]]_f$ bicycle Majorana code via a blind search. The same approach can be applied to search for other codes accordingly. In addition, we find that the other three types of codes proposed by Mackay et al. in Ref. [45] are not suitable for the fermionic LDPC code since one cannot find odd-weight logical Majorana operators similar to the Kitaev Majorana code.

C. Extracting odd-weight logical Majorana operators

We now describe how to identify odd-weight fermionic logical operators from the Majorana check matrix H constructed from check matrices $H_X = H_Z$ of a self-dual $[[n, k_q, d]]$ CSS code, that is,

$$H = \begin{pmatrix} H_\gamma & 0 \\ 0 & H_{\gamma'} \end{pmatrix} \quad (\text{S9})$$

where $H_\gamma = H_{\gamma'} = H_X = H_Z$. H is an $(n - k_q) \times 2n$ binary matrix with all row vectors linearly independent such that $\text{rank}(H) = n - k_q$. All logical operators correspond to nontrivial vectors in $\ker(H)/\text{im}(H^T)$. Let $S_L = \{\vec{v}_j | j = 1, \dots, 2k_q\}$ be a basis for $\ker H/\text{im}(H^T)$, where the weight of \vec{v}_j can be either even or odd [73]. An orthonormal set $\{\tilde{\gamma}_j\}_{j=1}^{2k_f}$ with $k_f \leq k_q$ consisting of the odd-weight vectors will be constructed from S_L . We show the procedure to construct the set constituting a basis for our code space of fermions in the following, generalizing the method in Ref. [60] to the \mathbb{F}_2 case.

If vectors in S_L all have even weight, then there do not exist odd-weight logical operators, since the addition of any two even-weight binary vectors yields an even-weight vector. Otherwise, there exists at least one odd-weight vector, say, \vec{v}_1 . We choose $\tilde{\gamma}_1 = \vec{v}_1$ as the first element in the odd-weight vector set and update the remaining $2k_q - 1$ vectors in S_L as $\vec{v}'_j \rightarrow \vec{v}_j - (\vec{v}_j \cdot \vec{v}_1) \vec{v}_1$. As a result, \vec{v}_1 is orthogonal to all the remaining vectors \vec{v}'_j ($j \geq 2$). We repeat this process until the remaining vectors are all of even weight, leading to an orthonormal set consisting of odd-weight

TABLE I. Comparison between the number of logical qubits and the number of logical complex fermion modes for different codes. d denotes the distance of the self-dual CSS codes.

Name	Bicycle code	EG(2, 4)	EG(2, 8)	EG(3, 2)	EG(3, 4)	PG(2, 4)	PG(2, 8)	PG(2, 16)	PG(2, 32)
n	100	30	126	42	630	16	64	256	1024
k_q	20	2	38	30	506	6	44	190	812
k_f	20	2	38	30	506	6	44	190	812
d	7	5	9	2	5	3	5	9	17

vectors. The algorithm is summarized in Algorithm 1. We note that this algorithm is similar to the algorithm in Ref. [74], which is aimed at constructing compatible symplectic basis from a weakly-self-dual CSS code.

Algorithm 1: Orthonormalization of $\{\vec{v}_j\}_{j=1}^{2k_q}$ over \mathbb{F}_2

Input: A set of binary vectors $\{\vec{v}_1, \vec{v}_2, \dots, \vec{v}_{2k_q}\}$ over \mathbb{F}_2

Output: The orthonormal basis of odd weight operators $\{\vec{\gamma}_j\}_{j=1}^{2k_f}$

```

1 Function Gram-Schmidt orthonormalization over  $\mathbb{F}_2(\{\vec{v}_1, \dots, \vec{v}_{2k_q}\})$ :
2    $\mathcal{B} \leftarrow \{\vec{v}_1, \dots, \vec{v}_{2k_q}\}$ ;                                     // Copy input vectors
3    $\mathcal{O} \leftarrow \emptyset$ ;                                           // Initialize orthogonal basis set
4   while  $\exists \vec{b}_i \in \mathcal{B}$  such that  $\vec{b}_i \cdot \vec{b}_i = 1$  do
5      $\mathcal{O} \leftarrow \mathcal{O} \cup \{\vec{b}_i\}$ ;
6      $\mathcal{B} \leftarrow \mathcal{B} \setminus \{\vec{b}_i\}$ ;
7     foreach  $\vec{b} \in \mathcal{B}$  do
8        $\vec{b} \leftarrow \vec{b} - (\vec{b} \cdot \vec{b}_i)\vec{b}_i$ ;
9     end
10  end
11  return  $\mathcal{O}$ ;

```

The following theorem provides a necessary and sufficient condition for the existence of an orthonormal basis for $\text{span}(S_L)$, i.e., an orthonormal basis consisting of odd-weight vectors.

Theorem .1. *Let G be a $2k_q \times 2k_q$ binary matrix defined by $G_{ij} = \vec{v}_i \cdot \vec{v}_j$ with $1 \leq i, j \leq 2k_q$. An orthonormal basis for $\text{span}(S_L)$ exists if and only if there exists an invertible matrix P such that*

$$PGP^T = I_{2k_q}. \quad (\text{S10})$$

Proof. If there exists an orthonormal basis $\{\vec{\gamma}_1, \dots, \vec{\gamma}_{2k_q}\}$ for the span, then we can write each vector in the basis as a linear combination of the vectors $\vec{v}_1, \dots, \vec{v}_{2k_q}$, that is, there exists a $2k_q \times 2k_q$ matrix P such that

$$\begin{pmatrix} \vec{\gamma}_1 \\ \vdots \\ \vec{\gamma}_{2k_q} \end{pmatrix} = P \begin{pmatrix} \vec{v}_1 \\ \vdots \\ \vec{v}_{2k_q} \end{pmatrix}. \quad (\text{S11})$$

Since $\{\vec{\gamma}_1, \dots, \vec{\gamma}_{2k_q}\}$ is orthonormal, we have $\vec{\gamma}_i \cdot \vec{\gamma}_j = \delta_{i,j} = \sum_{i',j'} P_{ii'} P_{jj'} \vec{v}_{i'} \cdot \vec{v}_{j'} = [PGP^T]_{ij}$, that is, $PGP^T = I_{2k_q}$.

Conversely, if there exists an invertible matrix P such that $PGP^T = I_{2k_q}$, we define a new basis $\{\vec{\gamma}_1, \dots, \vec{\gamma}_{2k_q}\}$ by

$$\begin{pmatrix} \vec{\gamma}_1 \\ \vdots \\ \vec{\gamma}_{2k_q} \end{pmatrix} = P \begin{pmatrix} \vec{v}_1 \\ \vdots \\ \vec{v}_{2k_q} \end{pmatrix}, \quad (\text{S12})$$

which clearly gives $\vec{\gamma}_i \cdot \vec{\gamma}_j = \delta_{i,j}$. Thus, $\{\vec{\gamma}_1, \dots, \vec{\gamma}_{2k_q}\}$ forms an orthonormal basis. \square

We numerically calculate the number of odd-weight logical Majorana operators forming k_f logical complex fermion modes for the check matrix H constructed based on bicycle codes, finite Euclidean geometry codes, and finite projective plane codes, and compare them with the number of logical qubits k_q for the corresponding self-dual CSS codes in Table I. We see that for all cases, the algorithm can efficiently find the same number of logical complex fermion modes as that of logical qubits, thus providing a high encoding rate.

S-2. FERMIONIC STATE TELEPORTATION

We now validate the quantum state teleportation circuit shown in Fig. 3(a) in the main text. Suppose that our fermionic LDPC code memory A encodes k_f logical complex fermion modes, and we want to transfer the logical information of the j th logical mode to a processor B , which is initialized in $|\bar{0}\rangle_B$. Let the logical state of A be $|\bar{\psi}\rangle_A$, and the state of the entire system $|\bar{\Psi}\rangle$ can be written as

$$|\bar{\Psi}\rangle = |\bar{\psi}\rangle_A |\bar{0}\rangle_B = (\bar{f} + \bar{c}_j^\dagger \bar{g}) |\text{vac}\rangle, \quad (\text{S13})$$

where \bar{c}_j^\dagger denotes the logical fermionic creation operator of the j th logical mode of code A , $\bar{h} = h(\bar{c}_1^\dagger, \dots, \bar{c}_{j-1}^\dagger, \bar{c}_{j+1}^\dagger, \dots, \bar{c}_{k_f}^\dagger)$ with $h = f, g$ represents a polynomial of the logical operators except the j th operator, and $|\text{vac}\rangle$ is the vacuum state. We prove that the logical state of the system will be $|\bar{\Psi}'\rangle = (\bar{f} + \bar{c}_B^\dagger \bar{g}) |\text{vac}\rangle$ after implementing the quantum state teleportation circuit, where \bar{c}_B^\dagger is the encoded logical creation operator of code B .

Let $\bar{c}_j^\dagger \equiv \frac{1}{2}(\bar{\gamma}_j + i\bar{\gamma}'_j)$ and $\bar{c}_B^\dagger \equiv \frac{1}{2}(\bar{\gamma}_B + i\bar{\gamma}'_B)$, the first step of the circuit is to perform the projective measurement of the joint parity operator $i\bar{\gamma}_j \bar{\gamma}_B$, resulting in the state proportional to

$$\begin{aligned} |\bar{\Psi}_1\rangle &\sim \frac{1 \pm i\bar{\gamma}_j \bar{\gamma}_B}{2} |\bar{\Psi}\rangle \\ &\sim (\bar{f} + \bar{c}_j^\dagger \bar{g} \pm i\bar{\gamma}_j \bar{\gamma}_B \bar{f} \pm i\bar{\gamma}_j \bar{\gamma}_B \bar{c}_j^\dagger \bar{g}) |\text{vac}\rangle \\ &\sim (\bar{f} + \bar{c}_j^\dagger \bar{g} \pm i\bar{\gamma}_j \bar{\gamma}_B \bar{f} \mp i\bar{\gamma}_B \bar{g}) |\text{vac}\rangle, \end{aligned} \quad (\text{S14})$$

where the last equation is due to the fact that $\bar{\gamma}_j = \bar{c}_j^\dagger + \bar{c}_j$. If the measurement result is $+1$, we proceed; otherwise, a Z gate $Z = \exp(i\pi \bar{c}_B^\dagger \bar{c}_B)$ is applied to the processor to derive the state

$$\begin{aligned} |\bar{\Psi}_2\rangle &= \exp(i\pi \bar{c}_B^\dagger \bar{c}_B) |\bar{\Psi}_1\rangle \\ &= (1 - 2\bar{c}_B^\dagger \bar{c}_B) |\bar{\Psi}_1\rangle \\ &\sim (\bar{f} + \bar{c}_j^\dagger \bar{g} + i\bar{\gamma}_j \bar{\gamma}_B \bar{f} - i\bar{\gamma}_B \bar{g}) |\text{vac}\rangle. \end{aligned} \quad (\text{S15})$$

We now perform the projective measurement of the particle number operator $\bar{c}_j^\dagger \bar{c}_j$, and the state becomes

$$\begin{aligned} |\bar{\Psi}_3\rangle &\sim \begin{cases} (1 - \bar{c}_j^\dagger \bar{c}_j) |\bar{\Psi}_2\rangle \\ \bar{c}_j^\dagger \bar{c}_j |\bar{\Psi}_2\rangle \end{cases} \\ &= \begin{cases} (\bar{f} - i\bar{\gamma}_B \bar{g}) |\text{vac}\rangle \\ (i\bar{\gamma}_j \bar{\gamma}_B \bar{f} + \bar{c}_j^\dagger \bar{g}) |\text{vac}\rangle \end{cases}, \end{aligned}$$

for the measurement result of 0 and 1, respectively. If the measurement result is 0, we simply proceed; otherwise, we apply the joint operator $i\bar{\gamma}_j \bar{\gamma}_B$ to get the state $|\bar{\Psi}_4\rangle = (\bar{f} - i\bar{\gamma}_B \bar{g}) |\text{vac}\rangle = (\bar{f} - i\bar{c}_B^\dagger \bar{g}) |\text{vac}\rangle$. After that, we apply a phase rotation gate $\bar{S} = \exp(i\frac{\pi}{2} \bar{c}_B^\dagger \bar{c}_B)$ to achieve the target state $|\bar{\Psi}'\rangle = (\bar{f} + \bar{c}_B^\dagger \bar{g}) |\text{vac}\rangle$.

One can easily derive that $i\bar{\gamma}_j \bar{\gamma}_B = -\bar{Z}_j (\overline{\text{Braid}(j, B)})^2$, where $\overline{\text{Braid}(j, B)} = \frac{1}{\sqrt{2}}(1 - \bar{\gamma}'_j \bar{\gamma}_B)$ is the logical braiding gate [15] and $\bar{Z}_j = i\bar{\gamma}_j \bar{\gamma}'_j$. Therefore, $i\bar{\gamma}_j \bar{\gamma}_B$ can be realized by applying two logical braiding gates and one logical Z gate as shown in Fig. 3(a), which can be realized transversally as shown in Fig. S2(b).

For two fermion gates, we need to transfer the information from two logical fermionic sites in the memory to two processors, and apply corresponding logical gates on the processors.

S-3. FERMIONIC LATTICE SURGERY

In the main text, we have introduced two methods to perform fermionic lattice surgery. In this section, we will analyze their overhead and demonstrate the fault-tolerance of the procedures.

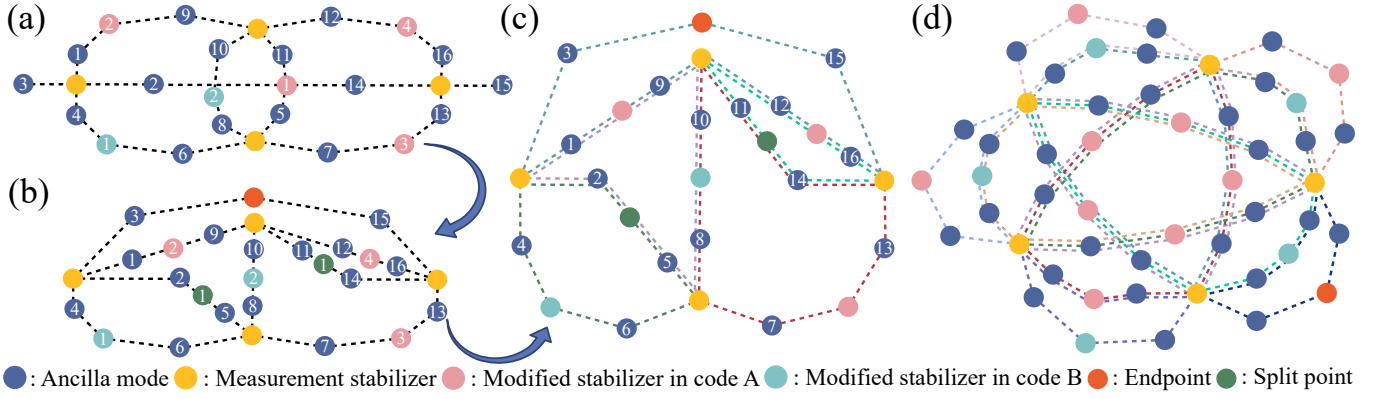


FIG. S3. Illustration of construction of gauge stabilizer generators in a general fermionic lattice surgery using method 2. (a) An initial graph. (b) A graph obtained by splitting modified stabilizers via adding more vertices, called split points, and by adding an endpoint that connects the ancilla Majorana operators introduced to ensure even-weight measurement stabilizers (node 3 and node 15). (c) Independent cycles, each represented by different colored closed paths. These figures correspond to the case shown in Fig. 6 in the main text. (d) Independent cycles for the case of performing fermionic lattice surgery between $PG(2, 8)$ and $d = 5$ fermionic color code.

- For each pair of ancilla Majorana operators that are introduced to ensure even-weight measurement stabilizers (e.g., node 3 and 15 in Fig. S3), we add an endpoint vertex between them and connect this vertex to the two ancilla mode vertices (see Fig. S3(b)).
- We refer to the vertices corresponding to measurement stabilizers as measurement vertices, the vertices corresponding to ancilla Majorana operators as ancilla vertices, and the modified stabilizers and the vertices added in the previous two steps as modified vertices.

Therefore, this graph contains $D_{AB} = \frac{D_A + D_B}{2}$ measurement vertices, $\sum_{i=1}^{N_A} m_{A,i} + \sum_{i=1}^{N_B} m_{B,i} + N_P$ ancilla vertices, $\sum_{i=1}^{N_A} \frac{1}{2} m_{A,i} + \sum_{i=1}^{N_B} \frac{1}{2} m_{B,i} + \frac{N_P}{2}$ modified vertices, and $2(\sum_{i=1}^{N_A} m_{A,i} + \sum_{i=1}^{N_B} m_{B,i} + N_P)$ edges, since each ancilla vertex connects two vertices. Since each measurement vertex has even degree, each modified vertex has degree two, and any two vertices can be connected by some path, this graph is an undirected Eulerian graph with a single connected component, indicating that it contains

$$|E| - |V| + 1 = \sum_{i=1}^{N_A} m_{A,i}/2 + \sum_{i=1}^{N_B} m_{B,i}/2 + N_P/2 - D_{AB} + 1 \quad (\text{S16})$$

independent cycles [75]. Here $|E|$ and $|V|$ denote the number of edges and vertices, respectively. The gauge stabilizer is then defined as the product of all ancilla Majorana operators on each independent cycle (see Fig. S3(c) and (d)).

The commutativity between measurement stabilizers and modified stabilizers is ensured by construction. We now verify that the gauge stabilizers are even-weight operators, and commute with measurement and modified stabilizers.

- Each path consists of a set of ancilla vertices, which are interlaced with measurement vertices and modified vertices. We note that each modified vertex connects exclusively to a pair of ancilla vertices on a cycle and each ancilla vertex connects one modified vertex, as depicted in Fig. S3(c). Therefore, the number of ancilla vertices in each cycle is twice the number of modified vertices, ensuring that gauge stabilizers are even-weight operators.
- The number of overlapped ancilla vertices between a gauge stabilizer and a modified stabilizer is even, and thus each gauge stabilizer commutes with all modified stabilizers.
- The number of ancilla vertices shared by a gauge stabilizer and a measurement stabilizer is always even. This is because, within the cycle of a gauge stabilizer, traversing a measurement vertex requires entering and exiting through two distinct ancilla vertices, as shown in Fig. S3(c) and (d).
- The gauge stabilizers commute with each other. If two cycles intersect at a vertex $\gamma_{a(b),i,j_1}$, they must pass through the modified vertex associated with $\gamma_{a(b),i,j_1}$. Consequently, these cycles must also intersect at the other vertex $\gamma'_{a(b),i,j_2}$ associated with this modified vertex, resulting in an even overlap between the two gauge stabilizers.

We now demonstrate that the merged code $\mathcal{C}_{\text{merged}}$ is a fermionic LDPC code with a low overhead. The number of ancilla fermions introduced is $\sum_i m_{A,i} + \sum_i m_{B,i} + N_P$, which is bounded by $\sum_i m_{A,i} + \sum_i m_{B,i} + D_{AB}$. This corresponds to a low-overhead construction, making this lattice surgery practical. The weight of measurement stabilizers is bounded due to the limited number of original stabilizers associated with each site. For the weight of gauge stabilizers, we numerically compute the maximum weight of the gauge stabilizers for 1000 randomly generated code pairs (A and B). Our results show that this weight scales as $[(|\bar{\gamma}_A| + |\bar{\gamma}_B|)/2]^{0.5}$, as illustrated in Fig. S4.

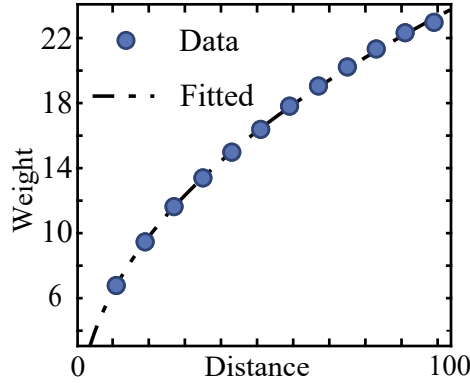


FIG. S4. Numerically computed maximum weight of the gauge stabilizers for 1000 randomly generated code pairs (A and B) with respect to the average weight of $\bar{\gamma}_A$ and $\bar{\gamma}_B$. The dotted-dashed line is power-law fit of the data.

The fault-tolerant measurement of the joint logical operator $i\bar{\gamma}_A\bar{\gamma}_B$ is due to the fact that this joint operator becomes a stabilizer of the merged code. To show this, we need to demonstrate that there exists a subset of gauge stabilizers, such that the product of these gauge stabilizers incorporates all ancilla Majorana operators, since the product of all measurement stabilizers contains $\bar{\gamma}_A\bar{\gamma}_B$ and all ancilla Majorana operators. The product of all ancilla modes corresponds to a big cycle containing all ancilla vertices, which can always be decomposed into a subset of the independent cycles found above. As a result, the product of all measurement stabilizers and this subset of gauge stabilizers leads to $i\bar{\gamma}_A\bar{\gamma}_B$. The measurement result of this operator is determined by the product of the measurement results of all measurement stabilizers and this subset of gauge stabilizers. In fact, only measurement results of measurement stabilizers are necessary since they are random due to their anticommutation with some original stabilizers in blocks A and B , while the gauge stabilizer results are always $+1$, since they belong to the stabilizer group of the original code.

In Fig. S3(d), we show an example depicting the results of independent cycle search for performing fermionic lattice surgery between $\text{PG}(2, 8)$ and a $d = 5$ fermionic color code.

Algorithm 2: Fermionic Lattice Surgery

Input: Codes A, B with stabilizers $\mathcal{S}_A, \mathcal{S}_B$, Logical fermionic site supports F_A, F_B
Output: Merged code $\mathcal{C}_{\text{merged}}$

- 1 \mathcal{A} (ancilla mode set) $\leftarrow \emptyset, \mathcal{S}_{\text{fix}} \leftarrow \{S \in \mathcal{S}_A \cup \mathcal{S}_B \mid \text{supp}(S) \cap (F_A \cup F_B) \neq \emptyset\}, \mathcal{S}_{\text{free}} \leftarrow (\mathcal{S}_A \cup \mathcal{S}_B) \setminus \mathcal{S}_{\text{fix}}$
- 2 **for** $S \in \mathcal{S}_{\text{fix}}$ **do**
- 3 **for** $i = 1$ **to** $\lfloor \frac{1}{2} |\text{supp}(S) \cap (F_A \cup F_B)| \rfloor$ **do**
- 4 introduce new ancilla site $a, \mathcal{A} \leftarrow \mathcal{A} \cup \{a\}, S \leftarrow Si\gamma_a\gamma'_a$
- 5 **end**
- 6 **end**
- 7 \mathcal{M} (measurement stabilizers) $\leftarrow \emptyset$
- 8 **foreach** $i \in 1 : \min(|F_A|, |F_B|)$ **do**
- 9 flag \leftarrow False, $M_i \leftarrow i\gamma_{F_A[i]}\gamma_{F_B[i]}$, Attach relevant ancillas to M_i without reuse
- 10 **if** $\text{wt}(M_i)$ is odd **then**
- 11 **if** flag is False **then**
- 12 introduce new ancilla site $a, \mathcal{A} \leftarrow \mathcal{A} \cup \{a\}, M_i \leftarrow M_i\gamma_a$, flag \leftarrow True
- 13 **else**
- 14 $M_i \leftarrow M_i\gamma'_a$, flag \leftarrow False
- 15 **end**
- 16 **end**
- 17 $\mathcal{M} \leftarrow \mathcal{M} \cup \{M_i\}$
- 18 **end**
- 19 Add pair operators for unpaired fermions
- 20 $G \leftarrow$ graph(\mathcal{A}), add edges for co-occurring ancillas in $\mathcal{S}_{\text{fix}} \cup \mathcal{M}$
- 21 \mathcal{G} (gauge stabilizers) $\leftarrow \{\prod_{v \in C} \gamma_v \mid C \in \text{Independent cycles}(G)\}$
- 22 **return** $\mathcal{C}(\mathcal{S}_{\text{free}} \cup \mathcal{S}_{\text{fix}} \cup \mathcal{M} \cup \mathcal{G})$

C. Fault-tolerance of fermionic lattice surgery

In this subsection, we will analyze the fault-tolerance of fermionic lattice surgery using the subsystem code formalism [65, 66]. The procedure's fault-tolerance is determined by the distance of the dressed logical operators, which will be defined shortly. For method 2 with a processor being a color code, we show that the distance of the dressed logical operators is at least the minimum weight of the original logical operators. For method 1, we provide numerical evidence demonstrating that the dressed logical distance is no smaller than the original logical distance.

A subsystem code is defined on $2n$ Majorana fermions by a gauge group \mathcal{G} , which is generated by a subset of Majorana string operators $\mathcal{G} \subset \text{Maj}(2n)$. The stabilizer group of \mathcal{G} is given by $\mathcal{Z}(\mathcal{G}) = \mathcal{C}(\mathcal{G}) \cap \mathcal{G}$, where $\mathcal{C}(\mathcal{G})$ is the centralizer group of \mathcal{G} . We define the bare logical operators as $\mathcal{L}_{\text{bare}} = \mathcal{C}(\mathcal{G}) \setminus \mathcal{G}$, the gauge operators as $\mathcal{L}_g = \mathcal{G} \setminus \mathcal{Z}(\mathcal{G})$, and the dressed logical operators as $\mathcal{L}_{\text{dressed}} = \{L \mid L = gl, g \in \mathcal{L}_g, l \in \mathcal{L}_{\text{bare}}\}$. The distance of the dressed logicals is defined as the minimum weight of all dressed logicals [65].

In our lattice surgery construction for method 2, the gauge group is defined as $\mathcal{G} = \langle \mathcal{S}_{\text{old}} \cup \mathcal{S}_{\text{merged}} \cup (\prod_j i\bar{\gamma}_j\bar{\gamma}'_j)\bar{\gamma}_B \rangle$, where \mathcal{S}_{old} denotes the union of stabilizer groups of codes A and B before merging, $\mathcal{S}_{\text{merged}}$ is the stabilizer group of the merged code, and $\prod_j i\bar{\gamma}_j\bar{\gamma}'_j$ is the product of all logical Majorana operators in codes A and B before merging. When $D_A = D_B$ ($D_A \equiv |\bar{\gamma}_A|$ and $D_B \equiv |\bar{\gamma}_B|$), the stabilizer group of the subsystem code is $\langle \mathcal{S}_{\text{old}} \cap \mathcal{S}_{\text{merged}} \rangle$, the gauge operators are $\langle (\prod_j i\bar{\gamma}_j\bar{\gamma}'_j)\bar{\gamma}_B, c_{B,1}, \dots, c_{B,D_B-1}, M_1, \dots, M_{D_B} \rangle$, and the bare logicals consist of all logical operators in codes A and B except $\bar{\gamma}_A$ and $\bar{\gamma}_B$. We note that this construction of gauge group does not apply to the fermionic lattice surgery using method 1, as more operators need to be included in the gauge group [65].

We now prove that the minimum weight of the dressed logicals is at least $\min\{d_A, d_B\}$, where d_A and d_B are the code distances of a fermionic LDPC code A and color code B , respectively. Consider an arbitrary dressed logical $L = gl$ with $g \in \mathcal{L}_g$ and $l \in \mathcal{L}_{\text{bare}}$, we analyze its weight $|L|$ according to the support of l .

If $\text{Supp}(l) \subset B$, where $\text{Supp}(\dots)$ denotes the set of physical fermionic sites supported by the operator, then $l \sim \bar{\gamma}'_B$. Since $(g)_B$ act only on γ -type Majorana modes, where $(\dots)_B$ denotes the operator supported on the Majorana modes of B , the weight $|l|$ cannot be reduced below D_B ,

For the case with $\text{Supp}(l) \subset A$, we decompose g as $g = l'mc_Ba$, where $m \in \langle M_1, \dots, M_{D_B} \rangle$, $c_B \in \langle c_{B,1}, \dots, c_{B,D_B-1} \rangle$, $l' \in \{\bar{\gamma}_A, I\}$, and $a \in \{(\prod_j i\bar{\gamma}_j\bar{\gamma}'_j)i\bar{\gamma}_B\bar{\gamma}_A, I\}$ (here if $l' = \bar{\gamma}_A$, then $a = (\prod_j i\bar{\gamma}_j\bar{\gamma}'_j)i\bar{\gamma}_B\bar{\gamma}_A$; otherwise,

both are equal to the identity operator). Then,

$$\begin{aligned}
|L| &= |ll'mc_Ba| \\
&\geq |(ll'mc_Ba)_A| + |(ll'mc_Ba)_B| \\
&= |(ll'ma)_A| + |(mc_B)_B| + |(a)_B| \\
&\geq |(ll'ma)_A| + |(m)_B| + |(a)_B| \\
&= |(ll'ma)_{A \cup B}| \\
&\geq |ll'a| \\
&\geq \min\{d_A, d_B\}.
\end{aligned} \tag{S17}$$

The third line holds because ll' is supported on A , $(mc_B)_B$ is supported on γ -type modes, and $(a)_B$ is supported on γ' -type modes. For the fourth line, if $(m)_B \sim \bar{\gamma}_B$, $|(m)_B c_B| \geq |(m)_B|$ since $|(m)_B|$ is the distance of the color code. Otherwise, since $\text{Supp}((m)_B) \subseteq \text{Supp}(\bar{\gamma}_B)$, we write $(m)_B = \bar{\gamma}_B o_B$ where $\text{Supp}(o_B) \subseteq \text{Supp}(\bar{\gamma}_B)$ and $\text{Supp}(o_B) \cap \text{Supp}((m)_B) = \emptyset$. Thus, $c_B(m)_B = c_B \bar{\gamma}_B o_B = \bar{\gamma}_{B,2} o_B$, where $\bar{\gamma}_{B,2} = c_B \bar{\gamma}_B$ is still a logical operator of the color code, whose weight cannot be smaller than $|\bar{\gamma}_B|$. Let us further write $o_B \sim \gamma_{B,i_1} \cdots \gamma_{B,i_r} \gamma_{B,i_{r+1}} \cdots \gamma_{B,i_j}$ where $0 \leq r \leq j \leq D_B$, $i_1, \dots, i_r \in \text{Supp}(\bar{\gamma}_{B,2})$, and $i_{r+1}, \dots, i_j \notin \text{Supp}(\bar{\gamma}_{B,2})$. Thus, $|\bar{\gamma}_{B,2} o_B| = |\bar{\gamma}_{B,2}| + j - 2r \geq |\bar{\gamma}_B| + j - 2r = |(m)_B| + 2(j - r) \geq |(m)_B|$. For the sixth line, if $al' \sim I$, then $|(ll'ma)_{A \cup B}| = |(lm)_{A \cup B}|$. We decompose l as $l = l_0 \gamma_{A,j_1} \cdots \gamma_{A,j_s}$ where l_0 does not contain any operator in $\{\gamma_{A,1}, \dots, \gamma_{A,D_A}\}$. We also have $(m)_{A \cup B} \sim \gamma_{A,i_1} \gamma_{B,i_1} \cdots \gamma_{A,i_p} \gamma_{B,i_p}$, where $0 \leq p \leq D_B$ and $1 \leq i_1, \dots, i_p \leq D_B$. Thus, multiplying m to l only changes $\gamma_{A,i}$ in l to $\gamma_{B,i}$ if it is present in m . Thus, $|(lm)_{A \cup B}| \geq |l| \geq \min\{d_A, d_B\}$. Similarly, when $l'a \sim (\prod_j \bar{\gamma}_j \bar{\gamma}'_j) \bar{\gamma}_B$, we have $|(ll'ma)_{A \cup B}| \geq |ll'a|$. It follows that $|ll'a| \geq |(a)_B| \geq \min\{d_A, d_B\}$.

If l contains operators in both codes A and B , then $l \sim \bar{\gamma}'_B l_A$ where $\text{Supp}(l_A) \subset A$. Then, $|L| = |gl| = |\bar{\gamma}'_B| + |gl_A| \geq |\bar{\gamma}'_B| + \min\{d_A, d_B\}$.

For method 1 for fermionic lattice surgery, we numerically calculate the distance of the dressed logical operators, and the results are summarized in the table below. We find that the dressed logical distance is consistently no smaller than the original logical distance.

Index	1	2	3	4	5	6
Code A	Steane code	$d = 5$ -Color code	PG(2, 4)	PG(2, 8)	DB(5)	DB(11)
Code B	$d = 5$ -Color code	$d = 7$ -Color code				
Distance	3	5	3	5	4	7

TABLE II. Distances of subsystem codes during fermionic lattice surgery using method 1. DB and PG denote the double-chain bicycle code and projective geometry code, respectively. DB(5) is the double-chain bicycle code with the code parameter $[[20, 4, 4]]_f$ generated by polynomials $1 + x^3$ and $x^2 + x^3$ [49]. DB(11) is the double-chain bicycle code with the code parameter $[[44, 4, 7]]_f$ generated by polynomials $1 + x^{10}$ and $x^2 + x^5$ [49].

S-4. DETAILS OF NUMERICAL SIMULATIONS

In this section, we will provide more details regarding calculations of logical failure rate of the fermionic LDPC memory and simulations of fermionic circuits discussed in the main text.

A. Noisy fermion memory

Error models

To evaluate the performance of the fermion-to-fermion LDPC code, we consider three types of error models, similar to the qubit case: code-capacity, phenomenological and circuit-level error models, as shown in Fig. S5 [61].

The code-capacity error model considers a single round of errors on fermion sites after initialization with noiseless stabilizer measurements, as illustrated in Fig. S5(a). This model represents the upper bound of code performance concerning these errors. For these errors, similar to the commonly used one-qubit depolarizing noise channel in qubits [76], we consider its fermionic version (Majorana depolarizing noise channel) at each fermionic site, described

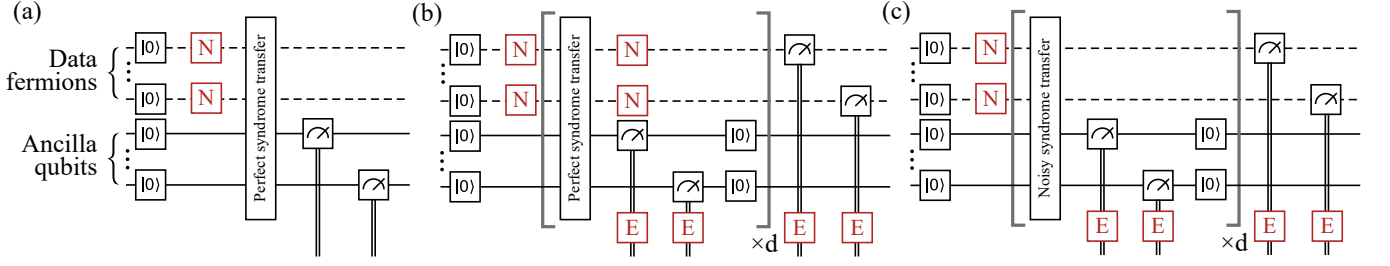


FIG. S5. Illustration of three error models: (a) code-capacity, (b) phenomenological, and (c) circuit-level error models. Here, the syndrome extraction circuit corresponds to the syndrome extraction transfer used to establish entanglement between data fermions and ancilla qubits, followed by measurements on the ancilla qubits. In (a) and (b), the syndrome extraction transfer is noiseless, while in (c), it is noisy as shown in Fig. S6. In all three cases, the initial states are physical $|0\rangle$ states for fermions. In (b) and (c), d rounds of syndrome extractions are applied and, a transversal measurement on all physical fermion modes in the particle-number basis is performed in the end.

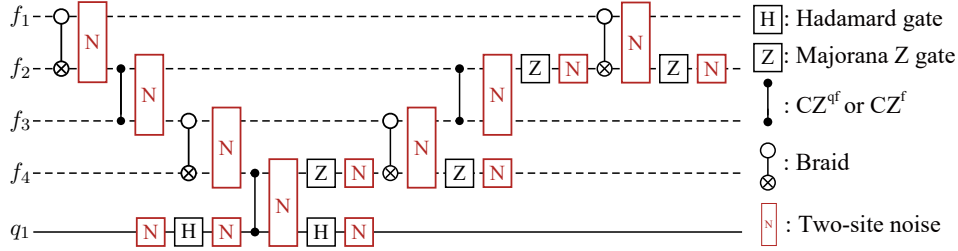


FIG. S6. Noisy fermionic syndrome extraction circuit for measuring the stabilizer $-\gamma_1\gamma_2\gamma_3\gamma_4$ at four fermionic sites assisted by a qubit [15].

by the following Kraus operators for a system with $2n$ Majorana modes:

$$\mathcal{E}_{\text{Maj}}^{(1)} = \left\{ \sqrt{1-p}I_j, \sqrt{\frac{p}{3}}\gamma_j, \sqrt{\frac{p}{3}}\gamma'_j, \sqrt{\frac{p}{3}}i\gamma_j\gamma'_j \right\}, \quad (\text{S18})$$

where $p/3$ denotes the probability of occurrence of either γ_j , γ'_j , or $\gamma_j\gamma'_j$ at fermionic site j . Figure S7 shows the logical failure rate with respect to the physical error rate for the finite projective geometry $\text{PG}(2,4)$ code, the finite Euclidean geometry $\text{EG}(2,4)$ code, the $[[100, 20, 7]]_f$ bicycle code, and three double-chain bicycle codes. We clearly see that the logical failure rate is significantly suppressed compared to the physical one according to the power law $p_L \sim p^\alpha$ with $\alpha \approx \lceil \frac{d}{2} \rceil$.

Compared with the code-capacity error model, the phenomenological error model accounts for syndrome extraction errors, as shown in Fig. S5(b). We consider d rounds of syndrome extractions, with each extraction followed by a round of single-fermion-site depolarizing noise channels. As the phenomenological error model does not include the specifics of the syndrome extraction circuit, it does not involve error propagation through entangling gates. Since decoders have a significant impact on the codes' performance, we here consider two decoders: the belief propagation and ordered-statistical decoding (BP+OSD) algorithm [77] and the Tesseract decoder [54] (see the following subsection for detailed discussion on decoders). Figure S8 illustrates the logical failure rate as a function of the physical error rate for the phenomenological error model for those codes using the two decoders. We see that the logical failure rate remains significantly suppressed compared to the physical one. While the results from both decoders generally follow the scaling $p_L \sim p^\alpha$, for most analyzed codes, the fitting error for the former decoder is larger than that of the latter, and the exponent α is smaller than $\lceil \frac{d}{2} \rceil$ for the former, whereas it is larger than $\lceil \frac{d}{2} \rceil$ for the latter. We attribute the suboptimal performance of the BP+OSD decoder to the presence of numerous short cycles with length $l < 6$ in the Tanner graph used for decoding [77]; for instance, phase errors $i\gamma\gamma'$ can lead to loops of length $l = 4$.

For the circuit-level simulation, we also consider the errors occurring in the syndrome extraction transfer circuit, in addition to measurement errors and a round of one-fermion-site depolarizing noise channels immediately following preparation, as shown in Fig. S5(c). In the syndrome extraction transfer circuit, a noise channel, parameterized by the error rate p , is applied immediately after each operation, including fermion, qubit, fermion-qubit, and reset operations (see Fig. S6). For one-site operations, we consider the one-qubit or one-fermion-site depolarizing noise depending on

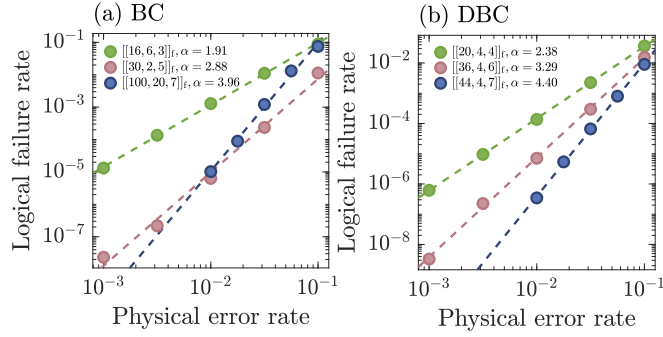


FIG. S7. Logistical failure rate with respect to physical error rate for the fermionic PG(2, 4) ($[[16, 6, 3]]_f$) code, the fermionic EG(2, 4) ($[[30, 2, 5]]_f$) code, the fermionic $[[100, 20, 7]]_f$ bicycle code in (a), and for three double-chain bicycle codes in (b), under code-capacity noise model. Here, the BP+OSD decoder is used. The error bars are hidden behind the data points. The dash-dotted lines—similarly depicted in Fig. S8, Fig. S9, and Fig. S10—are the linear fit of the four smallest data points.

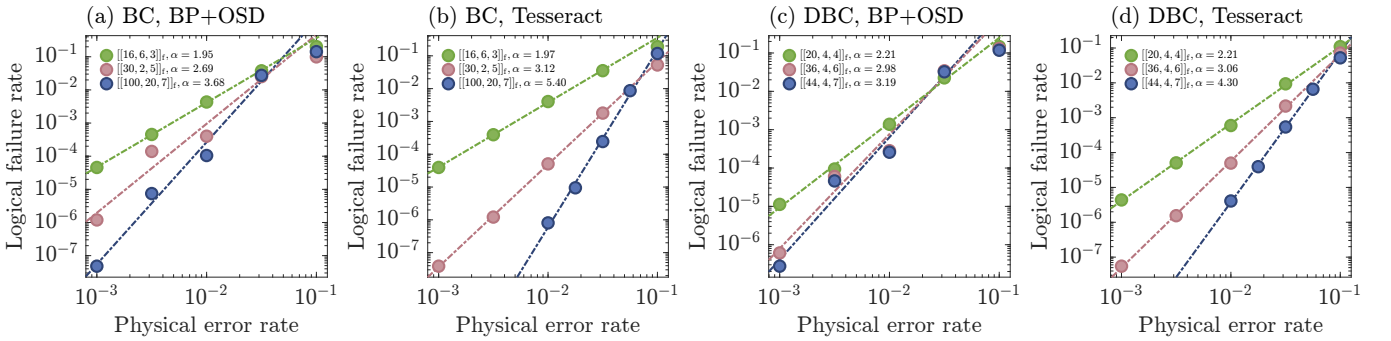


FIG. S8. Logistical failure rate as a function of physical error rate for the fermionic PG(2, 4) ($[[16, 6, 3]]_f$) code, the fermionic EG(2, 4) ($[[30, 2, 5]]_f$) code, the fermionic $[[100, 20, 7]]_f$ bicycle code in (a) and (b), and for three double-chain bicycle codes in (c) and (d), under phenomenological noise model. In (a) and (c), the BP+OSD decoder is used, whereas in (b) and (d), the Tesseract decoder is employed. The error bars are hidden behind the data points.

whether the operation is applied to an ancilla qubit or a fermion site. For two-site operations, we consider the two-site depolarizing noise. For example, when applied to two fermion sites, the two-fermion-site depolarizing noise is used:

$$\mathcal{E}_{\text{Maj}}^{(2)} = \left\{ \sqrt{1-p} I_1 I_2, \sqrt{\frac{p}{15}} I_1 \gamma_2, \sqrt{\frac{p}{15}} I_1 \gamma_2', \dots, \sqrt{\frac{p}{15}} \gamma_1 \gamma_1' \gamma_2 \gamma_2' \right\}. \quad (\text{S19})$$

If the two-site gate involves a qubit, then we consider a two-site mixed depolarizing noise obtained by replacing γ_2 , γ_2' , and $\gamma_2 \gamma_2'$ in the above channel by X , Y , and Z , respectively.

Figure S9 shows the results considering the circuit noise model. We see that the fitted α is significantly reduced for the PG(2, 4) and EG(2, 4) codes compared to the results under the phenomenological error model. For the $[[100, 20, 7]]_f$ bicycle code, the BP+OSD decoder reduces α to 2.27; in contrast, the Tesseract decoder maintains it at 3.74. Similarly, for the double-chain bicycle codes, the Tesseract decoder demonstrates superior performance, as indicated by α close to $\lfloor \frac{d}{2} \rfloor$ and the pseudo-threshold surpassing 0.1% for the $[[36, 4, 6]]_f$ and $[[44, 4, 7]]_f$ codes.

In Fig. S10, we provide the simulation results for the fermionic double-layer bivariate bicycle (BB) codes, double-layer twisted BB codes, and double-layer reflection codes under circuit-level noise model using the Tesseract decoder. We see that most codes exhibits the pseudo-threshold exceeding 0.1%.

In numerical calculations, similar to Python package stim, when decoders can give the correct prediction value for logical operators after performing $N_c = d$ syndrome measurement cycles (we set $N_c = d$ for the phenomenological and circuit-level error models), it is recorded as a correct event; otherwise, it is recorded as a failure. The probability of measurement error is on the same order of magnitude as the physical error rate; we set the probability of measurement error to $p/3$, where p represents the physical error rate. The logical error probability is given by $P_L = \frac{N_{\text{failure}}}{N_{\text{sample}}}$, where N_{failure} is the number of erroneous trials over total N_{sample} trials. By convention, the logical failure rate is defined as $p_L(p) = 1 - (1 - P_L)^{1/N_c} \approx P_L/N_c$, where P_L depends on the physical error rate p [37, 38]. The standard deviation

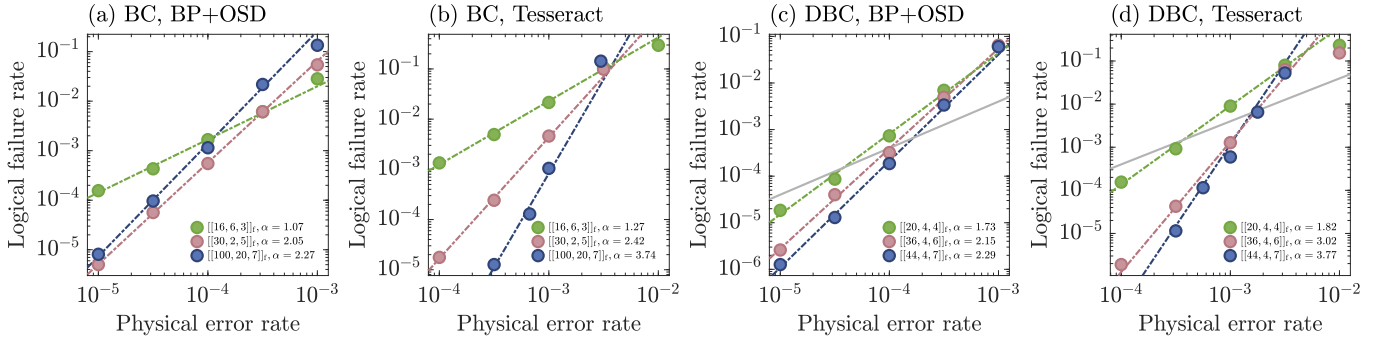


FIG. S9. Logical failure rate with respect to physical error rate for the PG(2, 4) ($[[16, 6, 3]]_f$) code, the EG(2, 4) ($[[30, 2, 5]]_f$) code, the $[[100, 20, 7]]_f$ bicycle code in (a) and (b), and for three double-chain bicycle codes in (c) and (d), under circuit noise model. In (a) and (c), the BP+OSD decoder is used, whereas in (b) and (d), the Tesseract decoder is employed. The error bars are hidden behind the data points. The grey lines in (c) and (d) represent the probability that an error occurs on at least one physical site.

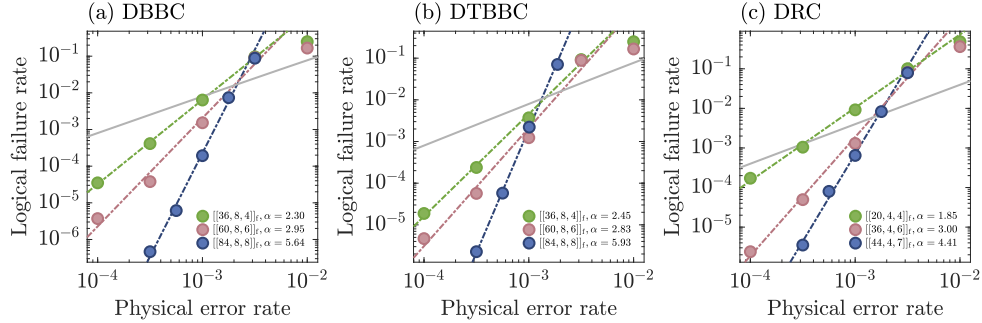


FIG. S10. Logical failure rate versus physical error rate obtained under circuit-level error model using the Tesseract decoder for (a) fermionic double-layer BB codes, (b) fermionic double-layer twisted BB codes, and (c) fermionic double-layer reflection codes. The grey lines represent the probability that an error occurs on at least one physical site.

of P_L is $\sigma_{P_L} = \sqrt{\frac{1}{N_{\text{sample}}} P_L (1 - P_L)}$ so that the standard deviation of p_L plotted as error bars in the numerical simulations of logical failure rate is $\sigma_{p_L} = (1/N_c)(1 - P_L)^{(1/N_c)-1} \sigma_{P_L}$ [37, 38]. We apply a self-adjusting strategy to determine the number of samples N_{sample} for each physical error rate p , which ensures a sufficient number of trials with σ_{p_L} below 10% of corresponding logical failure rate. The pseudo-threshold is defined as the physical error rate p_{th} , such that $p_L(p_{\text{th}}) = P(p_{\text{th}}, k)$ [38], where $P(p, k) = 1 - (1 - p)^k$ represents the probability that at least one of k physical fermion sites experiences an error.

Detector error model

With syndromes obtained by stabilizer measurements and transversal measurement results, we use a decoder to identify the errors that have occurred [78]. In addition to the measurement data, it is necessary to provide the decoder with a detector error model, which explains how errors activate the information captured by detectors. A detector error model is a data structure that encodes the structural information of noisy quantum circuits, including the spatiotemporal probability distribution of errors and their correlation effects on syndromes and logical operators, into a graph representation that can be parsed by decoders [78]. The decoder relies on this data format to understand the circuit structure accurately.

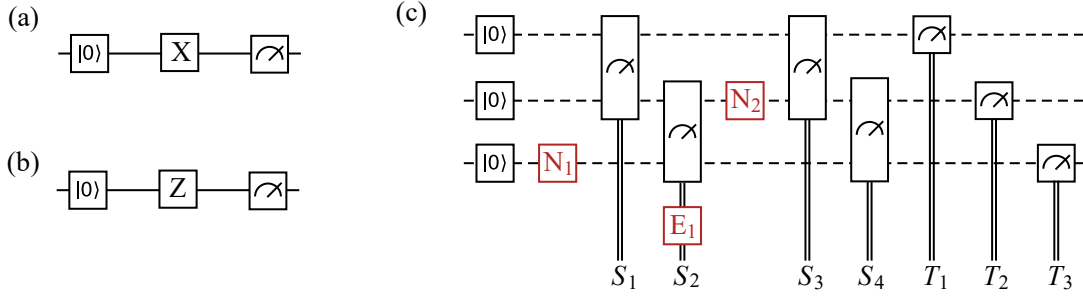


FIG. S11. (a) For the circuit, a detector is a measurement outcome in the Z basis, and an X error can trigger the detector, i.e., flip the value of the detector to -1 . (b) A Z error cannot trigger the detector. (c) We use a Majorana repetition code consisting of three fermion sites for demonstration of a detector error model. Two noises N_1 and N_2 and one measurement error E_1 are considered. S_1 and S_3 (S_2 and S_4) are the measurement outcomes of the stabilizer $-\gamma_1\gamma'_1\gamma_2\gamma'_2$ ($-\gamma_2\gamma'_2\gamma_3\gamma'_3$). T_j with $j = 1, 2, 3$ denotes the measurement outcome of the particle number operator at the j th physical fermion site.

To enhance readability, we use the following text format to describe a detector error model:

$$\begin{cases} \text{Error 1}(p_1) & D_1, D_2, \dots \\ \text{Error 2}(p_2) & D_2, L_1, \dots \\ \dots, & \end{cases} \quad (\text{S20})$$

where each line corresponds to an independent error event occurring with the probability specified by the symbol in the bracket, such as p_1 or p_2 . Detectors and logical observables triggered by the event are listed on the right-hand side, where D_j and L_j denote detectors and logical observables, respectively. A detector refers to the parity of a set of measurement outcomes in the circuit. For example, in Fig. S11(a), the measurement outcome in the Z basis constitutes a detector for a qubit state initialized in $|0\rangle$. An X error—an error event—can trigger the detector to yield -1 . Assuming that the X error is the sole trigger, if the detector reads -1 , the error's occurrence is confirmed. This detector cannot identify a Z error, as it does not trigger it (see Figure S11(b)). In general circuits, attention is required only if measurement outcomes expected to be consistent show inconsistency.

Next, we use a test circuit of a Majorana repetition code consisting of three fermion sites as an example to demonstrate how to derive the detector error model from a fermionic circuit. The code's stabilizer generators are $-\gamma_1\gamma'_1\gamma_2\gamma'_2$ and $-\gamma_2\gamma'_2\gamma_3\gamma'_3$. For simplicity, we consider three errors: a γ_3 error denoted as N_1 , a measurement error denoted as E_1 , and a depolarizing error denoted as N_2 , as illustrated in Fig. S11(c). Under ideal, noiseless conditions, the two stabilizers always remain at $+1$, and the values of consecutive syndrome measurements do not vary. However, an error can cause a change detectable by detectors. We therefore consider the following detectors: $D_1 = S_1$, $D_2 = S_1S_3$, $D_3 = S_3T_1T_2$, $D_4 = S_2$, $D_5 = S_2S_4$, and $D_6 = S_4T_2T_3$, where S_j with $j = 1, 2, 3, 4$ denote the syndrome extraction values and T_j with $j = 1, 2, 3$ denote the transversal measurement outcomes in the computational basis. The logical observable is defined by $L_1 = T_1T_2T_3$, which should ideally be $+1$ under noiseless conditions.

Deriving the detector error model requires us to analyze the events triggered by each independent error occurrence. When N_1 occurs, the stabilizers that anticommute with γ_3 flip sign, causing S_2 to flip sign, which triggers detector D_4 and the logical observable of L_1 . When E_1 occurs, detectors D_4 and D_5 are triggered. N_2 corresponds to a depolarizing noise described by the Kraus operators of $\{\sqrt{1-p}I, \sqrt{\frac{p}{3}}\gamma_2, \sqrt{\frac{p}{3}}i\gamma_2, \sqrt{\frac{p}{3}}\gamma'_2\}$. Such an error cannot be described by a single independent event, since the occurrence of the error of γ_2 indicates that other errors do not happen. We therefore need to express this noise channel in terms of three independent error channels: $\{\sqrt{1-p'}I, \sqrt{p'}\gamma_2\}$, $\{\sqrt{1-p'}I, \sqrt{p'}\gamma'_2\}$, $\{\sqrt{1-p'}I, \sqrt{p'}i\gamma_2\gamma'_2\}$. In the Kraus-operator formulation, it can be shown that the two are equivalent when $p' = \frac{1}{2}(1 - \sqrt{1 - \frac{4}{3}p})$. Thus, we decompose the channel of N_2 into three independent channels, representing errors of γ_2 , γ'_2 , and $i\gamma_2\gamma'_2$, respectively. Similarly, a two-site depolarizing noise can be decomposed into 15 independent two-term Kraus channels with each error occurring with the probability of $\frac{1}{2}(1 - (1 - \frac{16}{15}p)^{1/8}) \approx \frac{p}{15}$. The error of either γ_2 or γ'_2 triggers D_2 , D_5 , and L_1 , while the error of $i\gamma_2\gamma'_2$ triggers no events and thus can be ignored. We denote the occurrence probabilities of the four errors including N_1 , E_1 and the two independent errors caused by N_2 as p_1 , p_2 , p_3 , and p_4 , respectively (note that $p_3 = p_4$). The resulting detector

error model is as follows:

$$\begin{cases} \text{Error 1}(p_1) & D_4, L_1 \\ \text{Error 2}(p_2) & D_4, D_5 \\ \text{Error 3}(p_3) & D_2, D_5, L_1 \\ \text{Error 4}(p_3) & D_2, D_5, L_1. \end{cases} \quad (\text{S21})$$

To efficiently compute the detector error model for fermionic circuits, we extend the concept of the Pauli frame to the Majorana frame. Currently, most decoders can decode based on the detector error model without distinguishing the specific physical implementation of the underlying circuit. This enables the use of decoders for fermionic circuits similarly to their use for qubit circuits. We have incorporated the numerical method for generating detector error models for fermionic circuits into the Python package [78].

Decoder setups

In this work, we use two independent decoders: the BP+OSD algorithm [77], a most commonly used decoder for quantum LDPC codes, and the Tesseract decoder based on A^* search and beam search strategies [54].

For the former, we employ its Python package `stimbposd` implementation [77]. The core workflow of the BP-OSD algorithm is summarized as follows: It first converts a detector error model into a Tanner graph, an undirected graph, where vertices represent errors, detectors, or logical observables and each line in the detector error model corresponds to several edges with each edge indicating that an error triggers a detector or logical observable. After this, the BP algorithm is used to update the marginal probabilities iteratively of each error through N_{BP} iterations in total. This BP process provides the likelihood of each error occurring. Based on the results of the BP process, the OSD process sorts all errors in descending order of likelihood and selects the top k errors as highly probable occurrences. Furthermore, the algorithm selects multiple flips of some errors among w errors, i.e., assuming that they did not occur, and uses Gaussian elimination to solve which remaining errors need to occur to satisfy the detector occurrences. Here, w is called the OSD order. Finally, it calculates the probabilities of various solutions, select the one with the highest probability as the error pattern, and analyze whether logical observables flip under this error pattern. In our work, the configuration parameters for the BP+OSD decoder are set as follows: the number of BP iterations $N_{\text{BP}} = 100$, the OSD candidate set size $k = 200$, and the OSD search order $w = 8$ (sweeping mode).

The Tesseract decoder is a maximum likelihood estimation (MLE) decoder developed by Google Quantum AI [54], and we employ its open-source implementation as a benchmark for comparison. This decoder introduces heuristic guidance, directing the search direction through a precomputed heuristic function, prioritizing exploration of high-probability error patterns. Additionally, the decoder employs beam pruning strategies, retaining only the top k_{beam} candidate error patterns at each search level, balancing accuracy and efficiency. The parameters used in this work when calling this decoder include beam width $k_{\text{beam}} = 60$.

B. Fermionic circuit simulation

We now provide the details of Fig. 4 in the main text. There, we choose the fermionic $[[88, 4, 7]]_f$ double-chain bicycle code as the fermionic memory and use the four logical modes for simulation and two fermionic $[[37, 1, 7]]_f$ color codes as the processors. The memory is initialized in the $|\bar{0}\bar{1}\bar{0}\bar{1}\rangle$ state. We then perform multiple rounds of the circuit shown in Fig. 4(a), where each round represents a time step. To implement the tunneling gate or fSWAP gate between logical modes, we transfer the corresponding logical modes from the memory to the processors via fermionic lattice surgery, perform the gate on the processors, and then transfer the logical modes back to the memory. The processors are then reset to $|\bar{0}\bar{0}\rangle$ state, preparing them for the next tunneling or fSWAP gate. We apply the same circuit-level error model as described previously, with a physical error rate of $p = 10^{-4}$. We execute the circuit with and without error correction. For simplicity, we assume that onsite measurements in both Fig. 3(a) and Fig. 4(a) are noiseless. For all other cases, we account for circuit-level errors with d cycles of syndrome extraction followed by error correction. The decoder used here is the Tesseract decoder [54]. We track the expectation value of logical particle numbers at sites 1 and 4 at each time step to compare the simulation results of both scenarios.

In the main text, we employ the first method to perform fermionic lattice surgery. Here, in Fig. S12, we provide the simulation results achieved using the second method for lattice surgery.

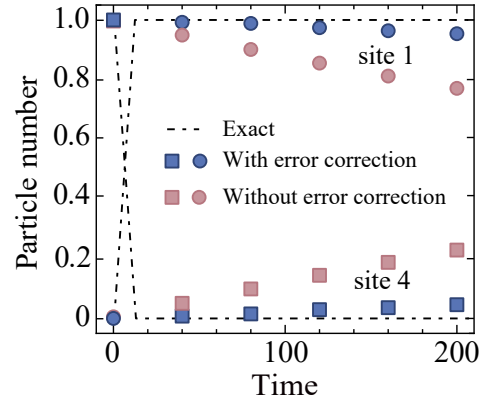


FIG. S12. The time evolution of logical particle numbers at sites 1 and 4, which are the same as in Fig. 4(b) except that the lattice surgery is performed using the second method. The error bars are hidden behind the symbols.